

CHARACTERIZATION OF SILICON CARBIDE COATINGS ON  
ZIRCALOY-4 SUBSTRATES

By

YOUSIF A. AL-OLAYYAN

A DISSERTATION PRESENTED TO THE GRADUATE SCHOOL  
OF THE UNIVERSITY OF FLORIDA IN PARTIAL FULFILLMENT  
OF THE REQUIREMENTS FOR THE DEGREE OF  
DOCTOR OF PHILOSOPHY

UNIVERSITY OF FLORIDA

2003

Copyright 2003

by

Yousif Al-Olayyan

Dedicated to my mother and my wife.

## ACKNOWLEDGMENTS

I would like to acknowledge and thank my advisor, Dr. Gerhard Fuchs, for his continuous and great support, guidance and advice. I am truly thankful to Dr. Ronald Baney for his much appreciated encouragement and for constructive discussions during our weekly project meetings. Thanks are due to Dr. Darryl Butt, Dr. Paul Holloway and James Tulenko for their advice and supervision. I also appreciate the help from Dr. Butt's group, especially Jairag Payyapilly, for their help in autoclave testing.

Thanks go to my company, Saudi Basic Industrial Corporation (SABIC), who offered me the scholarship and gave me this great chance for knowledge and achievement and also offered me a one year extension to fulfill my objective and finish my research work.

Finally thanks are due to my mother and wife, who missed me a lot, for their patience, love and support during my studies.

## TABLE OF CONTENTS

	<u>Page</u>
LIST OF TABLES .....	vii
LIST OF FIGURES .....	viii
ABSTRACT.....	xiii
CHAPTER	
1 INTRODUCTION .....	1
2 BACKGROUND .....	3
Corrosion of Zirconium Alloys.....	3
Silicon Carbide Coating.....	5
Adhesion of Coatings.....	10
Scratch Test.....	12
Factors Affecting the Adhesion .....	14
Film Thickness .....	14
Substrate Roughness .....	15
Aging Effects.....	16
Ion Implantation .....	16
Use of Interlayer .....	17
Substrate Hardness .....	17
Mechanical Properties of the Coatings .....	18
Work of Adhesion .....	18
Ultimate Tensile Shear Strength (UTSS) .....	23
Interface Chemical Reactions .....	25
Failure Modes in Ceramic Coatings .....	27
3 EXPERIMENTAL .....	30
Introduction.....	30
Sample Preparation .....	31
Silicon Carbide Coating.....	33
Thermal Stability Test .....	34
Hydrothermal Autoclave Test.....	36
Characterization of Coatings .....	37
SEM/ EDS .....	37

Roughness Measurements .....	38
Scratch Test .....	38
Indentation Test .....	39
X-ray Diffraction Analysis .....	40
Tensile Tests .....	41
 4 RESULTS .....	 43
X-ray Investigation of SiC Films.....	43
Film Thickness Effects .....	45
Substrate Surface Preparation Effects.....	51
Thermal Stability Tests .....	60
Hydrothermal Effects.....	63
Characterization of "Trimethylsilane" Coatings.....	65
Thermal Stresses in Autoclave .....	67
Ion Implantation Effects on Zircaloy-4 .....	69
Ultimate Tensile Shear Strength .....	71
Work of Adhesion.....	76
 5 DISCUSSION .....	 78
Adhesion of SiC Coatings to Zircaloy Substrate .....	78
Cracks in 5 $\mu\text{m}$ SiC Films.....	80
Effect of Substrate Surface Treatment.....	83
Work of Adhesion.....	85
Analytical Techniques for Coating Characterization.....	88
Ultimate Tensile Shear Strength of the Coatings.....	89
Failure Mechanisms of CVD SiC Coatings in Hydrothermal Test.....	90
 6 CONCLUSIONS AND FUTURE WORK .....	 101
LIST OF REFERENCES .....	103

## LIST OF TABLES

<u>Table</u>	<u>page</u>
2.1 Physical properties of Zircaloy-4.....	4
2.2 Modes of thin film decohesion. ....	29
3.1 Chemical composition of Zircaloy-4. ....	31
3.2 Sample preparation and coating procedure for all the groups. ....	35
3.3 Test conditions for scratch analysis of samples from group A. ....	39
4.1 Roughness of all samples surfaces of Group B before and after coating. ....	52
5.1 stresses data for debonding of SiC and SiO <sub>2</sub> films from Zircaloy substrate.....	98

## LIST OF FIGURES

<u>Figure</u>	<u>page</u>
2.1 Schematic diagram shows the description of CVD process. ....	6
2.2 Four steps that characterize the mechanisms of plasma CVD process [23]. ....	7
2.3 Schematic diagram of the assembly of the pull stud to the sample to be tested [46].	12
2.4 Photograph of a coated sample after pull-off test showing (a) good and clean pull, (b) partial failure at the film-epoxy interface [46]. ....	12
2.5 Illustration of the typical scratch test [50]. ....	13
2.6 Critical loads for decohesion of TiN coatings on three different qualities of steel as a function of coating thickness [53]. ....	15
2.7 Geometry of the spalled region used in the Thouless model [68]. There is a trapezoidal delamination region of length $L$ ahead of a scratch of width $2a$ . The sides of the spalled region are prescribed by radial cracks that make an angle $\beta$ with the scratch direction. ....	22
2.8 Illustration of the experimental technique (top). A typical schematic of the increase in crack density with the strain applied to metal substrate (bottom) [79]. ....	25
2.9 SEM image of the cross section of a Zr/SiC diffusion couple heat treated at 1100°C for 144 h [82]. ....	26
2.10 Ternary Zr-Si-C isothermal phase diagram at 1300°C [82]. ....	26
2.11 SEM of a buckled ZnO thin film on Si substrate [87]. ....	27
2.12 The configuration used in Evan's model for buckling, shows also the tensile stress concentration accompanies film buckling [79]. ....	28
3.1 Seven zircaloy-4 samples coated with SiC are encapsulated before they placed in box furnace for thermal treatment. ....	36
3.2 The autoclave system used for hydrothermal testing of SiC coatings (manufactured by Autoclave Engineers). ....	37
3.3 Cross section of implanted Zircaloy sample shows the location of indentation tests.	40



3.4 Two dog-bone samples. Tensile test paused at 30%strain. B2: Zircaloy-4 Coated with 1.5 $\mu$ m thick SiC film. Zr-4: Zircaloy specimen with no coating. ....	42
3.5 Dog bone samples were fixed manually in the SEM for cracks characterization.....	42
4.1 X-ray diffraction results for (a) coated and uncoated samples, (b) coated samples showing the corresponding peaks for zirconium and silicon carbide, (c) peaks correspond to zirconia. ....	44
4.2 SEM images of SiC films of 5 $\mu$ m thickness deposited on Zircaloy-4 substrate (a,b) top surface shows a "mud" pattern of the cracks, (c-f) cross section show the propagation of cracks through SiC film. ....	46
4.3 SEM images of SiC films of 1 $\mu$ m thickness deposited on Zircaloy-4 substrate (a, b) top surface, (c, d) cross section. ....	47
4.4 SEM micrographs of the scratch channels on the 1 $\mu$ m SiC film on Zircaloy-4. ....	48
4.5 Typical graphs of scratch test show (a) variation of normal force and tangential force as function of scratch length, (b) good agreement between friction measurement and acoustic emission detection in the scratch test. ....	49
4.6 Critical load as function of film thickness obtained from scratch test.....	50
4.7 SEM secondary electron and backscattered (BS) micrographs shows the morphology of coating failure due in scratch test (a) first delamination in the 1 $\mu$ m SiC film, (b) continuous delamination in the 5 $\mu$ m SiC film. ....	50
4.8 Typical profilometer measurement of roughness showing roughness data, 3D image and y-profile. ....	52
4.9 Typical secondary electrons and backscattered (BS) images of a coated surface on (a) and (b) 600 grit polished substrate, (c) and (d) 240 grit polished substrate. ....	53
4.10 Low and high magnification SEM image of the top surface of the SiC films (a) deposited on the as-received Zircaloy-4 sample, (b) deposited on grit blasted (high roughness) Zircaloy-4 substrate sample. ....	55
4.11 SEM images show the thickness and cracks on the oxide film of zircaloy-4 oxidized at 1200°C (a,b,c) top surface, (d,e,f) cross section.....	55
4.12 SEM images show the appearance of zirconia when Zircaloy exposed to 1200°C for 10 min in dry air. ....	56
4.13 SEM images for the cross section of oxidized Zircaloy-4 in dry air at (a) 500°C, (b) 750°C.....	57

4.14 Typical EDS spectrum of top surface of Zircaloy-4 coated with 1 $\mu\text{m}$ thick SiC film of group B samples.....	57
4.15 SEM micrographs of the scratch channels on the 1 $\mu\text{m}$ SiC film on Zircaloy. ....	58
4.16 Coated sample after scratch test shows adhesive failure (a) SEM SE and BS images of scratch track, (b) EDS spectrum from coated area, (c) EDS spectrum inside scratch track.....	59
4.17 Critical load of SiC coating failure as a function of substrate surface preparation for samples of Group B. ....	59
4.18 The variation of critical load with coating surface roughness. ....	60
4.19 SEM images of SiC coatings show detachment of the film around the stylus track. ....	60
4.20 SiC coatings after heat treatment at 350°C for 500 hrs in vacuum (a) SEM image of the top surface, (b) EDS spectrum.....	61
4.21 First scratch in the sample B2.....	62
4.22 Critical load of the failure of the heat treated SiC coating compared to as-coated samples. ....	62
4.23 Scratch channel of as-coated and heat-treated samples. ....	63
4.24 Weight loss of Zircaloy samples coated by 1 $\mu\text{m}$ SiC film and exposed to thermal and hydrothermal conditions. ....	64
4.25 SEM images of SiC coating after autoclave, shows the sequence of failure (1) blistering and cracks, (2) propagation of buckles, (3 &4) connection of adjacent buckles which lead to (5&6) complete spallation of the film. ....	65
4.26 SEM images for (a) 1.5 $\mu\text{m}$ thick SiC, (b) 3 $\mu\text{m}$ thick SiC film on Zircaloy-4 substrate.....	66
4.27 EDS spectrum for SiC films top surface with thickness (a) 1.5 $\mu\text{m}$ , (b) 3 $\mu\text{m}$ . ....	67
4.28 EDS for 3 micron thick SiC film on Zircaloy-4 substrate (a) before autoclave, (b) after autoclave testing.....	67
4.29 Photograph shows the variations in the coating surfaces.....	69
4.30 Oxygen content in SiC films after different thermal and hydrothermal treatments as analyzed by EDS. ....	69
4.31 Stress-strain curve of Zircaloy-4 substrate with and without implantation. ....	70

4.32 Rockwell (HRA 60kg) hardness of zircaloy-4 dog bones specimens with and without hydrocarbon implantation. ....	70
4.33 Vickers microindentation (Hv 1Kg) profile made to the cross section of the implanted Zircaloy-4 specimen. ....	71
4.34 Carbon content in SiC film before and after implantation as analyzed by (a) EDS, (b) AES.....	71
4.35 SiC Film thickness as measured by SEM. ....	72
4.36 Tensile test of Zircaloy-4 coated with 1.5 micron SiC film. The test was paused at 30% strain to measure crack spacing. ....	72
4.37 SEM micrographs of cracks caused by uniaxial tension at different strains (a) 0.5, (b) 2%, (c) 10%, (d) 30%. ....	73
4.38 The distribution of crack spacing, $\lambda$ , obtained at applied tensile strain of 1, 2, 10 and 30%.....	74
4.39 SEM micrograph shows detachment of SiC film at (a) 10% applied strain, (b) 2% applied strain. ....	74
5.1 SEM images shows adhesive failure of the SiC films around indentation hole caused by plastic deformation of the substrate in indentation test using Rockwell (HRA 60kg).....	79
5.2 Two SEM images show flaking of the film around scratch channel on 5 $\mu$ m thick SiC film on Zircaloy substrate.....	80
5.3 Plane view of channel "mud" cracks found in (a) SiC films of 5 $\mu$ m thickness on Zircaloy substrate in our work, (b) Silicon nitride film of 1 $\mu$ m thick reported on silicon substrates caused by tensile stresses [99]. ....	81
5.4 Growth of channel crack in the film. ....	81
5.5 SEM images show a cross section of SiC film where channel cracks were found to reach the interface. ....	82
5.6 Experimental data shows the effect of pre-cleaning on the interfacial toughness of DLC coatings deposited on different substrates [110]. ....	84
5.7 Low and high magnification SEM images show intergranular corrosion in zirconia layer after autoclave testing.....	85
5.8 Residual stresses in PE-CVD SiC coatings on steel vs. annealing time at 923K [113].87	

5.9 Zircaloy-4 thick sheet after thermal annealing (a) at 730°C showing the iron-chromium phase precipitated throughout the matrix, (b) at 900°C showing the iron-chromium phase precipitated into the grain boundaries (1200X) [116].	88
5.10 Weight loss of different types of reaction-bonded silicon carbide (RBSC) compared with CVD SiC after exposure at 360°C for 7 days in pure water. H, M and L refer to the amount of free silicon as High, medium and low respectively [126].	93
5.11 (a) schematic illustration for oxidation of substrate through cracks and pinholes, (b) SEM micrographs for SiC coatings at the early stages of failure in autoclave show film blistering.	94
5.12 SEM and EDS map analysis show the oxygen distribution in the areas where failure begins.	94
5.13 Line scan and quantitative EDS analysis of partially failed film after autoclave test shows higher oxygen contents on the SiC film than on bare Zircaloy-4 metal.	95
5.14 A schematic indicating the cracking and spalling phenomena that occur after buckling.	96
5.15 Schematic diagram shows the nucleation of separation at the undulation peak caused by tensile stresses [133].	99

Abstract of Dissertation Presented to the Graduate School  
of the University of Florida in Partial Fulfillment of the  
Requirements for the Degree of Doctor of Philosophy  
CHARACTERIZATION OF SILICON CARBIDE COATINGS ON ZIRCALOY-4  
SUBSTRATES

By

Yousif A. Al-Olayyan

August 2003

Chair: Gerhard Fuchs

Major Department: Materials Science and Engineering

The lifetime of light water reactor (LWR) fuels is limited by the corrosion and degradation of Zircaloy cladding in the high temperature and high pressure operating conditions. As the thickness of the oxide layer increases, stresses build up in the oxide layer due to density differences between the oxide and the zirconium metal which lead to degradation and spallation of the oxide layer. The main objective of this research is to form protective coatings on the Zircaloy clad to prevent or at least slow the oxidation which can allow higher burnup of the fuel resulting in major benefits in plant safety and economics.

Silicon carbide was identified as a candidate protective coating to reduce the corrosion and degradation of Zircaloy cladding. Silicon carbide coatings were deposited on Zircaloy substrates using plasma-assisted chemical vapor deposition (PE-CVD) and were found to be amorphous as determined by X-ray analysis.

Since the adhesion of the films to the substrate was the most important property of a coating, scratch tests were used to assess the adhesion. The effects of different

parameters on the test results including residual stresses, plastic deformation and friction between the stylus and the surface are discussed. Critical loads, characterized by continuous delamination of the SiC coatings deposited on Zircaloy-4, occurred at 0.5- 2.5 N. The experimental results indicated that all SiC coatings used in this project, without exception, showed an adhesive failure when tested by scratch and indentation tests. Plastic deformation of the substrate due to compressive stresses induced by the scratch stylus caused flaking of the films at the interface, which was attributed to the low interfacial toughness.

The effects of film thickness and substrate surface treatment on the quality and adhesion of SiC coatings were studied in detail. Thick films (5 $\mu$ m) exhibited extensive cracking. The scratch tests indicated higher adhesion with intermediate substrate surface roughness (240 grit) compared to finer (600 grit) or coarser (grit blasted) treatments. Pre-cleaning of the substrate surface provided a significant enhancement in adhesion. Heat treatment of the coatings was found to increase the adhesion due to the relief of compressive residual stresses in the film. Ion implantation of the substrate surface was found to significantly increase the hardness and strength of the Zircaloy material.

Autoclave testing was used to assess the integrity and corrosion protection under high temperature (350°C) and high pressure (3000 psi) conditions. None of the silicon carbide coatings survived these dynamic autoclave exposures. Failure in the autoclave was believed to be due to buckling and spallation of the highly compressed films.

Work of adhesion and ultimate tensile shear strength of the SiC coatings were evaluated using models from the literature. The work of adhesion (0.2-0.8 J/m<sup>2</sup>) and ultimate tensile shear strength (0.54-1.54 GPa) were measured for 1 $\mu$ m thick SiC films

on Zircaloy substrates which did agree with literature values for weak interfacial toughness coatings.

## CHAPTER 1 INTRODUCTION

Oxidation of zirconium alloy cladding is the primary limiting factor against the operational lifetime of light water reactors. The fuel rod cladding serves as the first protection barrier from fission products and is extremely important to the safety of nuclear plants. An improvement on Zircaloy oxidation resistance will reduce the number of cladding failures and extend the burn-up in nuclear reactors. A silicon carbide coating was proposed in this research to offer an economic means of extending the life of Zircaloy clad based on corrosion considerations.

A major technical issue for coating a metal with a ceramic coating is the development of a strong adhesive bond between the coating and the substrate. This research investigated the quality and adhesion of silicon carbide films on Zircaloy-4 substrates. Thermal and hydrothermal stability of SiC films were also investigated. A detailed study on the effect of film thickness and Zircaloy substrate surface treatments on the adhesion of silicon carbide was performed in this research.

Chapter 2 provides the background and literature review on Zirconium alloys oxidation, silicon carbide coatings and deposition techniques. The different factors affecting the adhesion and the techniques and problems of adhesion measurement are also presented. Models from the literature for evaluation of the mechanical properties of the film and interface were reviewed and presented in this chapter.



Chapter 3 presents the experimental procedure, materials used, and characterization techniques utilized to analyze and evaluate the different properties of the SiC coatings.

Chapter 4 presents all the results in this research. Results for adhesion measurements obtained by scratch testing and the SEM characterization of scratch channels are presented. Thermal and hydrothermal stability testing results of SiC coatings are presented. Calculations and results for work of adhesion and ultimate tensile strength of the coatings are also given in this chapter.

Discussion and interpretation of the results is presented in Chapter 5. The possible mechanisms of the SiC failure in autoclave testing were also presented and discussed in detail in this chapter. The overall conclusions and the future work are presented in Chapter 6.

## CHAPTER 2 BACKGROUND

### **Corrosion of Zirconium Alloys**

Zirconium has a close-packed hexagonal crystal structure ( $\alpha$ -phase) at room temperature and it transforms to the bcc structure ( $\beta$ -phase) at about 870°C. It resists most inorganic, organic acids and alkalis and it is attacked by fluoride ions, wet chlorine, concentrated sulfuric acid, ferric and cupric chlorides [1].

The alloys of zirconium were developed for use as cladding material in nuclear reactors because they have good mechanical strength and ductility at reactor service temperatures; low neutron absorption; sufficient corrosion resistance to withstand pressurized water and steam; and adequate heat conductivity [2, 3]. The high corrosion resistance of zirconium alloys results from the formation of dense protective stable oxide layer on the metal surface which continues to grow slowly and remain tightly adherent at temperatures up to 550°C [4]. As an added benefit, these properties are relatively stable even after extensive irradiation in a reactor core [5].

Zirconium-4 is one of the important Zr alloys and were developed specifically for nuclear reactor applications. It has been extensively used as a fuel cladding material in a pressurized water reactors (PWR) where the alloy is exposed to the high temperature 350°C and high pressures (10-15 MPa) water environment. It contains the strong alpha stabilizers tin and oxygen and the beta stabilizers iron, chromium and nickel. Most alloying elements exist in the alloy as intermetallic compounds. In the conditions of use,

Zr oxidizes at the surfaces into zirconia [2]. The physical properties of Zircaloy-4 are given in Table 2.1.

Table 2.1 Physical properties of Zircaloy-4.

Property	Value
Minimum tensile strength	413 MPa
Minimum 0.2% yield strength	241 MPa
Elongation in 50mm	20%
Poisson's ratio at ambient temperature	0.37
Density	6.56 gm/cm <sup>3</sup>
Coefficient of thermal expansion at 25°C	$6.0 \times 10^{-6} \text{ }^{\circ}\text{C}^{-1}$
Melting point, T <sub>m</sub>	2100°C

Source: [4]

The corrosion rate of zirconium alloys is one of the major controlling parameters for the design of water reactor fuel element. Corrosion of zirconium alloys in hot pressurized water has been studied in detail [6-12]. In the growth of the dense oxide, the volume of Zr expands approximately 2.5 times when Zr is oxidized to ZrO<sub>2</sub>. This would induce the compressive residual stresses to ZrO<sub>2</sub> film because it is coherent to Zr and the stabilized tetragonal ZrO<sub>2</sub> layer which is stabilized at higher temperatures (>1250°C). These stresses are ultimately responsible for the spalling of the thick layers, have an effect on the whole deformation of the metal, and could favor the stabilization of the different crystallographic phases of zirconia. The stresses also lead to the breakaway transition and induce changes in the initial kinetics through the modification of the diffusion coefficient in the oxide. The corrosion rate is generally high when no tetragonal layer is observed [2, 8].

The oxidation kinetics of zirconium alloys are generally divided into two main parts separated by a transition. Prior to the transition, the corrosion rate is cubic or parabolic and the formed oxide is dense, composed mainly of monoclinic and tetragonal zirconia crystallites. After the transition, the oxidation rate increases rapidly and becomes

linear. Most of the oxide layers formed after the transition are porous, composed exclusively of m-ZrO<sub>2</sub> crystallites [7]. The transition occurs when the oxide thickness reaches about 2 to 4  $\mu\text{m}$  and leads to degradation of the initial dense protective film into a partially porous layer [10].

Corrosion resistance of Zircaloy-4 was improved by decreasing Sn and increasing Fe contents, and was attributed to an increase of the thickness of the tetragonal ZrO<sub>2</sub> layer [8]. The corrosion rate of zirconium alloys was found to increase with irradiation [9, 13, 14]. Toughening of zirconia due to stress induced transformation from tetragonal to monoclinic at crack tips is also an additional strengthening of the oxide film [15, 16].

### **Silicon Carbide Coating**

The silicon carbide coatings offer excellent potential to prevent the oxidation and hydriding of the Zircaloy cladding. Thin films of silicon carbide and silicon-carbon alloys are of great scientific and technological interest, since these materials exhibit outstanding properties, such as good mechanical strength, high hardness, high thermal conductivity and very high thermal stability [17-20]. Their applications may range from protective coatings against the corrosion of steel to micro electronic devices and from X-ray mask materials to the protection of fusion reactor walls, among others. These films can be deposited by a variety of techniques, such as laser-assisted deposition, dynamic ion mixing, plasma-enhanced chemical vapor deposition, magnetron sputtering, and many others [21].

Chemical vapor deposition is one of the best coating technologies to prepare high quality SiC films on large areas [17]. It is a technique for synthesizing materials in which chemical components in vapor phase react to form a solid film at the substrate surface.

The occurrence of a chemical reaction, which starts in the vapor phase, is essential for thin film growth in this technique [22]. Figure 2.1 shows the basics of CVD where gaseous reactants, called precursors, are introduced into a reactor in which the heated substrate is placed. On the surface, or in the vicinity of the surface, of the substrate, chemical reactions will occur and, as a result, a solid material is deposited as a thin film. The chemical bonds of, for example, silane, is cracked such that Si or SiH radicals are formed which are able to crack more silane molecules before reaching the substrate surface. The gaseous reaction products are then pumped away from the reactor. One of the most common methods to activate a CVD process is to use heat (called thermally activated CVD).

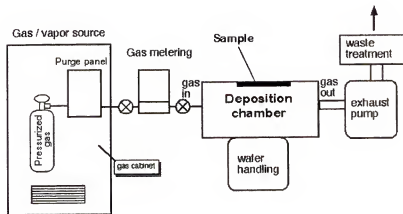


Figure 2.1 Schematic diagram shows the description of CVD process.

Another way of activating the process is to use plasma or a laser. Plasma enhanced chemical vapor deposition PE-CVD, for example, is one of the CVD techniques which has the ability to deposit films at low substrate temperatures. This was achieved primarily by lowering the activation energy through the formation of excited reactant species which allow the forward reaction to proceed at lower substrate temperatures [22].

In general, the deposition mechanisms for a plasma enhanced CVD process can be qualitatively divided into four major steps [23], as shown in Figure 2.2. Step 1 includes the initial electron-impact reactions between electron and reactant gases to form ions and radical reactive. Next, in step 2, the reactive species are transported from the plasma to the substrate surface concurrently with the occurrence of many elastic and inelastic collisions in both the plasma and sheath regions, classified as ion and radical generation steps.

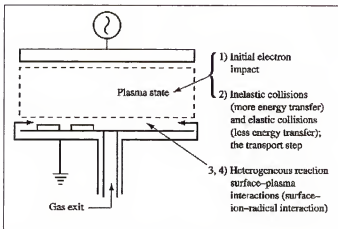


Figure 2.2 Four steps that characterize the mechanisms of plasma CVD process [23].

Step 3 is the absorption and/or reaction of reactive species onto the substrate surface. Finally, in step 4, the reactive species and/or reaction products incorporate into the deposited films or re-emit from surface back to the gas phase. Significant roles are played by ion bombardment and various reactions between ions and radicals with the depositing surface in the sheath region. The latter two steps are very important and critically affect film properties such as conformality, density, stress, and "impurity" incorporation.

Amorphous silicon carbide (a-SiC) films are generally produced by plasma enhanced chemical vapor deposition PE-CVD using the mixture of silane and methane

( $\text{CH}_4 + \text{SiH}_4$ ) at relatively low substrate temperature ( $< 400^\circ\text{C}$ ) [20, 24-30]. Other precursors are also used to produce amorphous SiC by the same technique, for example, methyltrichlorosilane (MTS:  $\text{CH}_3\text{SiCl}_3$ ) [21, 31-33], tetramethylsilane (TMS) [34, 35] and monomethylsilane ( $\text{CH}_3\text{SiH}_3$ ).

Crystalline SiC has a wider band gap and higher conductivity than amorphous SiC [19]. Crystalline SiC films can be grown by chemical vapor deposition but only at relatively high substrate temperatures ( $> 1100^\circ\text{C}$ ) [34, 35]. Methyltrichlorosilane (MTS:  $\text{CH}_3\text{SiCl}_3$ ) is mainly used to produce crystalline SiC by CVD technique at high temperatures [17, 18, 36-39]. They can be produced [20] from gas at  $2400^\circ\text{C}$  or from liquid at  $1500^\circ\text{C}$ .

The requirement for high temperatures for crystalline SiC production limits its application. High temperature deposition of SiC ( $> 1100^\circ\text{C}$ ) required to produce crystalline CVD may cause atoms diffusion from the substrate into the growing film, leading to defect formation [34]. Furthermore, high stresses are developed during cooling to room temperature due to the thermal expansion mismatch between films and substrate [40]. Deposition at high temperatures may also change the properties of the metallic substrate that were developed by previous heat treatment.

The alternative method to avoid high temperature deposition is to prepare amorphous films at low temperature followed by thermal annealing in vacuum in the range of  $900\text{--}1000^\circ\text{C}$ . This treatment leads to the formation of crystalline SiC films through homogeneous nucleation of fine crystal grains. Thermal treatment was also found to reduce or eliminate hydrogen incorporation in the film [34]. Partially crystalline SiC films produced by PE-CVD were observed after thermal treatment at  $600\text{--}700^\circ\text{C}$  [19, 41].

One of the major advantages of plasma assisted deposition processing is the flexibility for depositing films with desirable chemical and physical properties by varying deposition parameters such as filament temperature, substrate temperature, rf power, gas flow rate, pressure and gas mixture [23, 25, 26, 28, 33, 42].

Amorphous SiC films deposited by PE-CVD at 200-400°C using silane-ethelyne gas mixture were found [43] to have compressive stresses of about 2 GPa. These stresses were attributed to the incorporation of hydrogen in the film, where 40 at% of hydrogen was detected in the film. This high concentration of hydrogen also was the reason for low density of the film [27]. Annealing of the film in vacuum above 400°C eliminated the hydrogen and reversed the stresses from compressive to tensile.

Generally, the stresses in the thin films are divided into two types; intrinsic and extrinsic. The intrinsic stresses are formed during the formation and growth of the thin films. Ion bombardment by sputtered atoms and working gas densifies thin films, results in high compressive stresses. The microvoids may arise when byproducts during deposition escape as gasses and the lateral diffusion of atoms evolves too slowly to fill all the gaps, resulting in tensile stresses. The other causes of intrinsic stresses include volume change due to phase transformation and mismatch in lattices parameters.

Extrinsic stresses, on the other hand, are formed from unintended external factors, such as thermal stresses due to the mismatch in coefficient of thermal expansion between two materials.



### Adhesion of Coatings

Adhesion is a critical property of a coating. A major technical challenge for coating a metal with a ceramic protection system is to develop a cohesive bond between the two dissimilar materials. It is essential to obtain strong adhesion between ceramic coatings and substrates that can withstand the severe environments found in a reactor, such as stresses/pressures of 15 MPa (2,200 psi) and temperatures of about 345°C (650F).

Adhesion as defined by Mittal (as cited in Brown [44] ) can be divided into three categories: basic or fundamental adhesion, thermodynamic or reversible adhesion, and experimental or practical adhesion.

Basic or fundamental adhesion is related to the nature and strength of the binding forces between the two materials. Ionic, covalent, coordinate, metallic, hydrogen and van der Waals forces are the main types of bonding in materials. However, this basic definition of adhesion is not very helpful since it can not practically be easily used to test the adhesion of the coatings.

Thermodynamic or reversible adhesion is defined in terms of the work of adhesion,  $W_{AB}$ , by this equation:

$$W_{AB} = \gamma_A + \gamma_B - \gamma_{AB} \quad (2.1)$$

where  $\gamma_A$  and  $\gamma_B$  are the specific surface free energies of material A and B respectively, and  $\gamma_{AB}$  is the interfacial specific free energy. If at least one of the phases involved is a liquid, this equation may be useful. That is, surface tension of liquid and contact angles could be easily measured. Thus, if  $\theta$  is the contact angle and  $\gamma_B$  is taken to be the specific surface free energy of the liquid phase, then:

$$W_{AB} = \gamma_B (1 + \cos \theta). \quad (2.2)$$

Mittal identified experimental or practical adhesion with terms such as adhesion strength which could be measured by some method in which the maximum force per unit area required to separate a coating from its substrate is determined.

Experimental values of adhesion may not have direct relevance to the basic or fundamental adhesion because of the interactions with the substrate and the variation inherent to each type of test techniques. Consequently, different methods for measuring adhesion often give different values for the same coating-substrate systems.

In the late 1950s, adherence testing of ceramic coatings on metallic substrate was done by rude methods. For example, a ball with known weight was dropped at a right angle from specific height onto the coated surface. If no fracture occurred in the coating, its adherence to its substrate was considered acceptable. On the other hand, if fracture was observed, the area of coating detached from the substrate was taken as a measure for the adhesion of the coating to its substrate.

Several methods and techniques were developed for adhesion testing [45]. The most important and common techniques used for adhesion measurements are the scratch test and the pull-off test.

In the pull-off test, as shown in Figure 2.3, an aluminum stud with 2-5mm diameter head is bonded to the film surface using an epoxy and then pulled off with a constantly increasing force, normal to the substrate surface [46]. The force required to remove the film from the substrate is referred to as the pull strength. Multiple pulls are usually performed on each sample to determine the average adhesion across the sample surface. For a system with a low bond strength or work of adhesion, a small defect can initiate failure of the film. The load at which the stud is pulled from the sample is representative

of the film adhesion only if the film is pulled cleanly from the entire head area of the stud as shown in Figure 2.3(a).

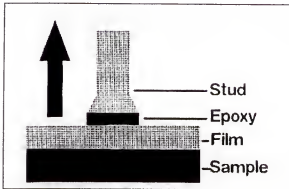


Figure 2.3 Schematic diagram of the assembly of the pull stud to the sample to be tested [46].

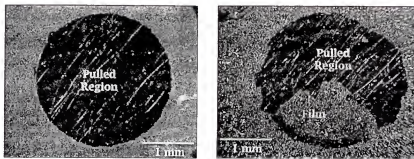


Figure 2.4 Photograph of a coated sample after pull-off test showing (a) good and clean pull, (b) partial failure at the film-epoxy interface [46].

The limitation of this technique is that the maximum adhesion that can be measured must be less than the strength of the bonding material [45]. Therefore, this technique is suitable only when the adhesion between the film and substrate is poor. Figure 2.4(b) shows a failure at the film-epoxy interface as a result of poor epoxy bonding.

### Scratch Test

This is one of the most popular methods of testing adhesion strength of thin films which has long been used [46-50] to assess the adhesion of thin hard coatings and is a useful tool for coating development and characterization. Benjamin and Weaver [51, 52] used the scratch test to study a very wide range of metals on glass substrates. Perry [53,

54] used the scratch test for the measurement of adhesion of CVD and PVD hard coatings on different types of steel.

The scratch-test method [50] consists, as shown in Figure 2.5, of the generation of scratches with a spherical stylus (generally Rockwell C diamond, tip radius  $200\mu\text{m}$ ) which is drawn with progressive loading at a constant speed across the coating surface to be tested. The critical load ( $L_c$ ) is defined as the smallest load at which a recognizable failure occurs.

The plastic deformation of the substrate occurred during the scratch test and this deformation induced a shearing force at the film-substrate interface in front of the indenter. When a critical load is reached, this shearing force is equal to the interfacial shear strength and thus complete removal of the film from the substrate occurred. The scratch test is considered to be a standard adhesion test and the critical load ( $L_c$ ) is generally taken as a measure of adhesion. The critical load is the load for which either increased acoustic emission is generated or a change in friction is detected.

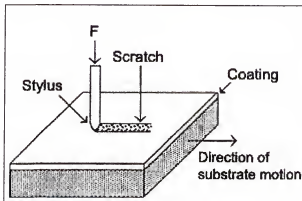


Figure 2.5 Illustration of the typical scratch test [50].

However, the adhesion strength obtained from the scratch test is only qualitative measurement [47]. The critical loads depend on the mechanical strength (adhesion, cohesion) of a coating-substrate composite and also on several other parameters: some of

them are related to the test itself, while others are related to the coating-substrate system. The test specific parameters of the scratch test include loading rate, scratching speed, and indenter tip radius and indenter material. The coating-substrate specific parameters include substrate hardness and roughness, coating hardness and roughness, coating thickness, friction coefficient between coating and indenter and, internal stresses in the coating [46]. Benjamin and Weaver [51] showed that the critical load obtained from the scratch method is not only influenced by the film properties but also the substrate. In their study, silver films were deposited on many different substrates having different hardness levels and they found variation in critical load values. They have suggested that the hardness of the substrate is the most important factor.

Therefore, the “adhesion” obtained from the scratch test must be a qualitative measurement for the (relative) adhesion of coating substrate, and the adhesions from two different coating/substrate systems will be incomparable.

### **Factors Affecting the Adhesion**

Various factors and techniques are currently used to enhance the adhesion between ceramic thin films and metal substrates. However, some of these factors affect the measurement of critical load in the scratch test and are not necessarily related directly to the adhesion.

#### **Film Thickness**

Generally, the critical normal load was found to increase with increasing thickness [45, 53-55] (for example, see Figure 2.6). However, it is not clear whether the apparent increase in critical load with coating thickness represents a real increase or a decrease in adhesion [56]. In the scratch test, the stress required for coating detachment is transmitted through the coating; therefore, thicker layers may require a greater surface stress to

achieve the same shear at or near the interface, thus showing higher critical loads [48, 56]. That is, using a scratch test method, for a given load, the scratch stylus is believed to induce lower stresses on the coating substrate interface as the film thickness increases. It was also believed [57] that the increase in adhesion with film thickness does not represent an increase in adhesion but it is a feature of buckling failure mode.

Adhesion of coatings tested by the scraping method was found to decrease with increasing film thickness [58].

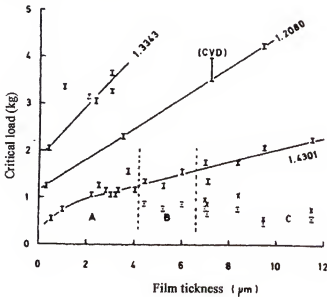


Figure 2.6 Critical loads for decohesion of TiN coatings on three different qualities of steel as a function of coating thickness [53].

### Substrate Roughness

One of the methods to improve the adhesion of thin films is to modify the topography of the substrate surface. Grit blasting of the substrate surface was found to enhance the adhesion [59] and it was concluded that adhesion has its maximum value at a specified degree of roughness. Adhesion of coatings tested by the scraping method was found to be increased by roughening of the substrate surface by grinding and also by etching of the substrate surface [58]. Valli and Makela [48] have reported that the

coefficient of friction between the stylus tip and the coating surface is a dominant factor affecting the results of scratch test. However, they have found no effect of roughening the substrate surface on adhesion itself even though the critical load increased with gas nitriding of the substrate. They have attributed this increase in adhesion to an improvement in load support afforded by harder surface layer.

### **Aging Effects**

Aging of the coating has an effect on adhesion of thin films. Benjamin and Weaver [52, 60] have studied the aging effects of different coating systems. They found an increase of adhesion with time after deposition and they attributed this effect to the formation of an oxide intermediate layer which produces a form of chemical bonding. They also found that, for oxygen active metals, adhesion is enhanced if there is enough oxygen during deposition to form an intermediate oxide layer.

### **Ion Implantation**

Ion implantation has been used for a long time to increase the adhesion strength of thin films to their substrates in metal-ceramic systems [46, 58, 61-64]. The work of adhesion increases by lowering the interfacial energy. Roughening effect and providing a nitride case depth were the main cause of the adhesion enhancement in ion implantation

The adhesion of TiN coatings has been improved [58] by a pre-nitriding of the substrate. However, not all ions are equally effective in ion implantation. For example, nickel implantation between iron film and alumina was found to degrade the adhesion [46] while iron and chromium ions enhance it. Generally, the smoothly graded interface leads to good film substrate adhesion. Valli [48] has found an increase in critical load by nitriding the substrate and attributed this increase to the hardening effect of the substrate.

The effect of ion implantation on the microstructure and mechanical properties of the substrate was found [65] to extend to large distances below the implanted surface. The increase of the surface hardness by ion implantation was attributed to solid solution strengthening, dispersion strengthening, increasing dislocation density and grain boundary strengthening due to the formation of sub-grains within the original grain structure.

### **Use of Interlayer**

Interlayer has been used to improve the adhesion of the coatings by reducing the elastic and thermal mismatch between film and substrate. The use of 150 nm thick Ti interlayer was found [66] to improve the adhesion of TiN films on Steel substrate due to a better chemical bond of Ti to the TiN film. The adhesion of thin SiC films deposited by PE-CVD on steel was enhanced by using TiN interlayer [49]. It was also found [67] that introducing a 1 nm thick intermediate layer of NiPt between NiO film and Pt substrate, which was introduced by heat treatment of the composite, has increased the ultimate shear strength by a factor of four.

### **Substrate Hardness**

Benjamin and Weaver [51] showed that the critical load obtained from scratch method is not only influenced by the film properties but also the substrate. In their study, silver films deposited on many different substrates having different hardness levels found variation in critical load values. They have suggested that the hardness of the substrate is the most important factor.



### **Mechanical Properties of the Coatings**

The scratch test is commonly used in the characterization of the adhesion strength of the hard thin films. However, few models have been proposed and developed to relate the experimental data of the adhesion test to the mechanical properties of the film and interface such as shear stress, interfacial toughness and work of adhesion.

The scratch test, as previously described, is a simple means of introducing a quantity of mechanical force or energy by stressing the coating under and around the moving stylus sufficient to detach the film. This has been used in the development of some models, either in terms of providing a critical interfacial shear stress [51, 52, 60] or elastic residual stresses [68, 69] which provides a driving force for delamination and spalling of the film or by providing the additional elastic energy required to satisfy the energy balance criterion for producing new surfaces due to film decohesion [70]. Analytical formulas for an approximate evaluation of the normal and interfacial stresses responsible for films peeling and blistering was developed by Suhir [71, 72] in a single and multilayered films. Impression tests using wedges [73], cones and spheres have also been used to measure the adhesion between thin films and ductile substrates. The size of delamination due to indenter impression has been used to measure the interfacial toughness.

#### **Work of Adhesion**

The work of adhesion,  $W_{AD}$ , measured by different mechanical tests is not the same as the thermodynamic "fundamental" adhesion. Most of the destructive tests used to measure the fracture energy,  $G$ , includes the work dissipated in the plastic deformation in the film and substrate,  $W_d$ , as well as the thermodynamic work of adhesion,  $W_{AD}$  [74]:

$$G = W_{AD} + W_d$$

It was reported [75, 76] that  $W_d$  is much greater than  $W_{AD}$ , which makes the estimate of the fundamental work of adhesion very difficult. Therefore, it is not possible to extract the true adhesive energy from the total energy measured. All of the adhesion tests and models for measurement of the work of adhesion use some external driving force or stored energy to cause the delamination of the film from the substrate. The amount of this energy is taken as the practical work of adhesion.

Laugier [70] has developed a model to calculate the work of adhesion,  $W_{AD}$ , of ceramic films from scratch tests and applied it for some selected materials with encouraging results. The theory is based on the energy balance criterion where, for coating detachment to occur, the stored elastic energy in the deformed coating must be large enough to generate two new surfaces at the interface.

According to his model, the work of adhesion required to debond a length  $\Delta x$  of the coating is equal to the stored elastic energy ahead of the indenter:

$$W_{AD} = \frac{h[\sigma(x)]^2}{2E} \quad (2.3)$$

where  $h$  is coating thickness,  $E$  is the Young's modulus of the coating and  $\sigma(x)$  is the total stresses in the coating which is equal to the coating internal residual stresses  $\sigma(x)_{int}$  plus the applied stresses  $\sigma(x)_{appl}$ .

The applied stress is function of the applied load,  $P$ , and the coefficient of friction,  $f$ , due to the sliding indenter:

$$\sigma(x)_{appl.} = \frac{P}{2\pi a^2} \left\{ (4 + \nu_s) \frac{3\pi f}{8} - (1 - 2\nu_s) \right\} \quad (2.4)$$

where  $\nu_s$  is the Poisson's ratio for the substrate and  $a$  is the radius of the contact surface.

Bull and Rickerby [77] have used a different approach to modeling the scratch test. The model is based on the determination of total frictional forces in a scratch test between the indenter and the coating surface due to compressive and shear stresses.

At a critical load of coating detachment,  $L_c$ , the relationship with the work of adhesion was found to be:

$$L_c = \frac{\pi d^2}{8} \left( \frac{2EW_{AD}}{h} \right)^{1/2} \quad (2.5)$$

where  $d$  is the track width. They have used this model to calculate the work of adhesion for 2-3  $\mu\text{m}$  thick TiN films on many types of steel.

Venkataraman et al. [69] have also used the critical load and the geometry of the delaminated area to determine the work of adhesion of hard thin films. They relates the stresses ahead of the sliding indenter to the strain energy released during film detachment and consequently determined the work of adhesion and interfacial toughness. The assumption made by other models [51, 52, 70] that the radius of the indenter tip must be large compared to the film thickness is not required in this model.

With the application of contact mechanics theory, the strain energy,  $G_i$ , released when the film flakes off was expressed as

$$G_i = \sum \left( \frac{\tau_{ij}^2}{2\mu} t + \frac{\sigma_y^2}{2E} t \right) \quad (2.6)$$

where  $\mu$  is the shear modulus of the film,  $t$  is the film thickness,  $\tau$  is the shear stress associated with the tangential force ( $fL_c$ ) acting with the indenter movement and  $\sigma$  is the normal acting stresses. A mathematical model was used [69] to calculate the normal and shear stresses from the critical load of scratch test and the geometry of delaminated region.

The work of adhesion will be equal to twice the strain energy released when film debonds which gives:

$$W_{AD}=2G_i$$

Therefore, the fracture toughness can be calculated using fracture mechanics, such that:

$$K_I = \sqrt{\frac{2\mu G_i}{1-\nu}} \quad (2.7)$$

The model was used to determine the work of adhesion and interfacial toughness of 1.2  $\mu\text{m}$  thick Pt film on NiO substrate and found a reasonable agreement when compared to the values from other methods.

The fracture toughness of the film and interface were determined [78] from periodic crack measurements. When decohesion of the film starts cracking proceeds in a periodic crack manner and allow for the calculation of the lower bound to interface toughness,  $\Gamma_i$ , from:

$$\epsilon_i = \left(\frac{2\Gamma_i}{E_f h}\right)^{1/2} \quad (2.8)$$

where  $\epsilon_i$  is the strain at crack saturation when the film is fully attached to the substrate,  $h$  is film thickness and  $E_f$  is the Young's modulus of the film.

The interface toughness was calculated [78] for a 1 $\mu\text{m}$  thick DLC film deposited on a steel substrate and found to be 150  $\text{Jm}^{-2}$  at 7% strain (just before the start of decohesion).

The interfacial toughness of thin brittle films was also determined by Thouless [68] using the geometry of the spall in scratch tests and it was found that the spall volume is

inversely proportional to the fourth root of the interfacial toughness. The interfacial toughness,  $\Gamma$ , was shown to be related to the geometry of the spall by:

$$\frac{\Gamma}{Et} \approx 0.35 \left( \frac{t}{L} \right)^4 \quad (2.9)$$

where  $t$  is the film thickness,  $L$  is the length of spall as shown in Figure 2.7 and  $E$  is the Young's modulus of the film.

This model also gave an approximate value for the critical buckling load,  $P_{cr}$ :

$$P_{cr} \approx 1.7 \frac{Et^3}{L} \left( \tan \beta + \frac{2a}{L} \right) \quad (2.10)$$

where  $a$  and  $\beta$  are geometrical parameters shown in Figure 2.7.

This model was used to compute the interfacial toughness between 1.2  $\mu\text{m}$  thick Pt film and NiO substrate and was found to be about  $\Gamma = 0.14 \text{ Jm}^{-2}$ .

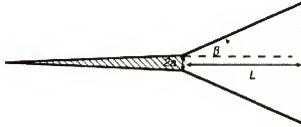


Figure 2.7 Geometry of the spalled region used in the Thouless model [68]. There is a trapezoidal delamination region of length  $L$  ahead of a scratch of width  $2a$ . The sides of the spalled region are prescribed by radial cracks that make an angle  $\beta$  with the scratch direction.

Benjamin and Weaver [51, 52, 60, 68] developed a model to study the adhesion of wide range of metals on the glass substrate and analyze the effect of substrate hardness and other properties on the adhesion using the scratch test technique. They have expressed the adhesion as the shearing force required to remove the film and assumed

that the coating substrate interface is subjected to a shearing force responsible for failure caused by the sliding stylus by the expressions [60]:

$$F = \frac{aH_v}{\sqrt{r^2 - a^2}} \quad (2.11)$$

where  $H_v$  is Vickers hardness of the substrate,  $r$  is the stylus tip radius and  $a$  is scratch channel width given by:

$$a = \sqrt{\frac{L}{\pi H_v}} \quad (2.12)$$

where  $L$  is the applied load, assuming  $a \ll r$ , the approximate relation will be:

$$F = \sqrt{\frac{LH_v}{\pi r^2}} \quad (2.13)$$

They have used this model to study a wide range of metallic films on a hard glass substrate.

### **Ultimate Tensile Shear Strength (UTSS)**

This technique, called the periodic cracking method was proposed by Argwal and Raj [79] to measure the ultimate shear strength of metal-ceramic interface. It has been applied to many ceramic/metal systems such as  $\text{SiO}_2/\text{Cu}$  [79] and  $\text{NiO}/\text{Pt}$  [67], DLC films on steel substrate [78] and also to both  $\text{SiOx}/\text{Au}$  and  $\text{SiO}/\text{Cu}$  [80] and on  $\text{TiN}/\text{Stainless Steel}$  [81].

The method, as described by Argwal and Raj [79], is illustrated in Figure 2.8 After deposition of ceramic films on metal substrates, the coated sample is pulled uniaxially. As the metal is plastically stretched, the ceramic film develops cracks that are oriented transverse to the pulling direction. The density of the cracks (the number per unit length) increases as more and more plastic strains are applied to the metal substrate. Eventually,

the crack density reaches a constant value and is not influenced by further plastic deformation of the metal. The ultimate shear strength of the metal-ceramic interface is related to the tensile fracture strength of the ceramic film and the largest spacing between the cracks; both of these quantities are measured in this technique. This technique is particularly suitable for application to metal-ceramic systems.

If the ceramic film is assumed to respond elastically to the applied loads, then the fracture strength of the film can be calculated from the Hook's law:

$$\sigma_f = E \varepsilon_f \quad (2.14)$$

where  $\varepsilon_f$  is the fracture strain of the film and  $E$  is the Young's modulus of the ceramic film.

The normal tensile stresses in the thin film are related to the shear stresses at the interface through simple force equilibrium equation [80]:

$$\sigma(x) = \frac{1}{\delta} \int_0^x \tau dx \quad (2.15)$$

where  $\sigma(x)$  is the tensile stresses in the film,  $\delta$  is the thickness of the film,  $\tau$  is the shear stresses at the interface and  $x$  is the coordinate along the interface with origin at the crack. From this equation, the ultimate shear strength at the interface is obtained as [79] as:

$$\tau_{max} = \frac{\pi \sigma_f \delta}{\lambda} \quad (2.16)$$

where  $\lambda$  is the maximum crack spacing in the film when the crack density becomes constant and  $\pi$  is the integration constant resulted from sinusoidal stress distribution assumption.

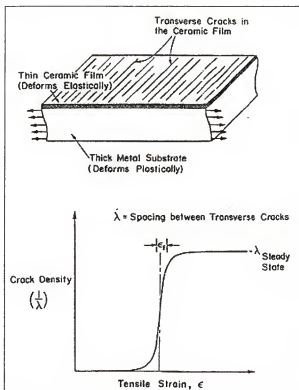


Figure 2.8 Illustration of the experimental technique (top). A typical schematic of the increase in crack density with the strain applied to metal substrate (bottom) [79].

### Interface Chemical Reactions

Most of the reactions at the interface were found to occur at much higher temperatures than that used in this research. Diffusion reactions between Zr/SiC were studied at 900-1100 °C [82]. The reaction of Zr with SiC led to the formation of layered structure of  $\text{ZrC}/\text{Zr}_5\text{Si}_3\text{C}/\text{Zr}_2\text{SiC}/\text{ZrC}_x$  compounds in the diffusion zone consistent with local equilibrium in the ternary Zr-Si-C phase diagram. In general, metals which form stable metal carbides, like Zr, show the tendency to form layered structures in the diffusion zone. A typical SEM image of the diffusion couple SiC/Zr heat treated at 1100°C for 144 hrs is shown in Figure 2.9. The diffusion path is shown in the Zr-Si-C phase diagram at 1300 °C (Figure 2.10). The stable ZrC was found to be the dominant phase in the reaction zone.



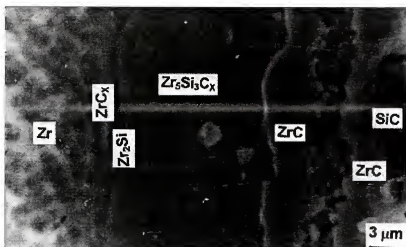


Figure 2.9 SEM image of the cross section of a Zr/SiC diffusion couple heat treated at 1100°C for 144 h [82].

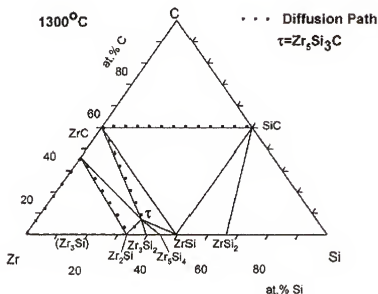


Figure 2.10 Ternary Zr-Si-C isothermal phase diagram at 1300°C [82].

Similar reactions were found in the interface reactions between SiC/Ti when studied at 900°C [83]. The chemical composition of the reaction zone between the SiC and Ti was found to be a two-phase zone, which consists largely of  $\text{TiC}_x$  crystals within a matrix of  $\text{Ti}_5\text{Si}_3\text{C}$ . In Zr/Si multilayer, the first phase formed by solid-state reaction was

found [84] to be  $\text{ZrSi}$  followed by the formation of  $\text{ZrSi}_2$ . Hot implantation of nitrogen at  $700^\circ\text{C}$ , was also found to form  $\text{ZrC}$  [85].

Due to the low deposition temperature used in this project ( $\sim 350^\circ\text{C}$ ), it is not expected to have any interaction at the interface, and if any reactions would occur, it may happen only within 2-3 nm atoms depth which would be very difficult to characterize.

### **Failure Modes in Ceramic Coatings**

The failure modes of thin brittle films were studied extensively by Evans and co-workers [86-88] and by many others [27, 89] and are summarized in Table 2.2. Films and coatings that formed by vapor deposition process are subjected to residual stresses during the deposition process and also during the cooling process when there is a thermal expansion mismatch between film and substrate. Residual tensile stress tends to induce coating fracture normal to the interface, while the residual compressive stresses provides a driving force for buckling and eventual spallation [27, 89]. Tensile residual stresses in the coating causes through thickness cracks which may develop from pre-existing defects in the film which may also generate shear stresses along the interface that lead to the decohesion. On the other hand, compressive residual stresses promote propagation of cracks along the interface and film buckling as shown in Figure 2.11.

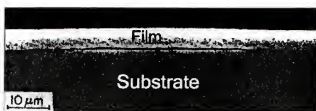


Figure 2.11 SEM of a buckled ZnO thin film on Si substrate [87].

Buckling can occurs when there is pre-existing separation between the film substrate according to the configuration shown in the Figure 2.12, and when the compressive stresses exceeds a critical value given by [87]:

$$\sigma_c = \left[ \frac{\pi E_c}{12(1 - \nu_c^2)} \right] \left( \frac{t}{c} \right)^2 \quad (2.17)$$

where  $E_c$  and  $\nu_c$  are, respectively, the Young's modulus and Poisson's ratio of the coating,  $t$  is the film thickness and  $c$  is the separation radius between film and substrate.

Spallation of buckled region requires that the delaminataion crack deflect upward in the film in a direction normal to that of the interface. The radial component of the strains in the buckled region at the bottom edge is expected to initiate and cause the spall, due to large tensile component. These radial strains were analyzed to obtain the critical conditions for spallation to occur. The critical value of the initial separation radius and film thickness for delaminataion to occur for a given compressed stresses is [79]:

$$\left( \frac{c}{t} \right) = 1.92 \sqrt{\frac{\sigma_o}{E}} \quad (2.18)$$

Contaminated surfaces can be a source of initial separation. For the delaminataion to propagate and cause spallation, a critical value of  $\sigma_c \sqrt{t}$  must be exceeded.

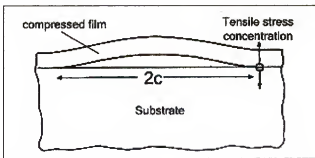


Figure 2.12 The configuration used in Evan's model for buckling, shows also the tensile stress concentration accompanies film buckling [79].

Table 2.2 Modes of thin film decohesion.

Residual stress	Film	Substrate	Interface bonding	Decohesion mechanism(s)
Tensile	Brittle	Ductile	Good	Film cracking: No decohesion
			Poor	Film cracking → interface decohesion
	Ductile	Brittle	Good	Edge decohesion in substrate
			Poor	Edge decohesion at interface
	Ductile	Ductile	Good	Edge decohesion at interface
			Poor	Film/ substrate splitting → Substrate decohesion
	Brittle	Brittle	Poor	Edge decohesion at interface (higher film toughness)
			Good	Film cracking → Interface decohesion
Compressive	Brittle	Ductile	Good	Buckle propagation in film
			Poor	Buckle propagation at interface
	Ductile/ Brittle	Brittle	Good	Substrate splitting
			Poor	Buckle propagation at interface
	Ductile	Ductile	Good	No decohesion
			Poor	Buckle propagation at interface

Source: [90]

The purpose of this study is to characterize the adhesion and quality of ceramic coatings applied to metal (Zircaloy) substrate with different substrate conditions and to provide a detailed analysis of coated substrates before and after exposing to corrosion environment. The microstructure and mechanical properties of the ceramic coatings will be measured and correlation with corrosion protection will be determined.

## CHAPTER 3 EXPERIMENTAL

### Introduction

The major technical challenge for coating ceramic films with metal substrates is to develop and maintain a strong bond between the low thermal expansion brittle ceramic coatings to the high thermal expansion ductile metal substrate. In this case, it is also important to ensure the resistance of the protective film to the thermal and hydrothermal conditions. The adhesion, stability and properties were examined for silicon carbide coatings on Zircaloy substrate. Experimental strategies to examine and address this challenge include:

- Investigation of SiC coatings with different film thicknesses.
- Use of different substrate conditions to provide improved adhesion of the ceramic coating to the metal substrate.
- The use of a compliant interlayer to relieve expansion mismatch stresses.
- Determine the stability of coating under thermal exposure.
- Determine the mechanical properties such as interfacial shear strength, toughness and work of adhesion of the coating system by applying models from literature with data from experimental work.
- Investigation of the resistance of coating to the high temperature (350°C) and high pressure (300psi) hydrothermal conditions.

This chapter describes the Zircaloy -4 samples used for the experiments with their composition and surface preparations. The SiC coatings, thermal, mechanical and hydrothermal tests details were presented. The various equipment and analytical techniques used during the experiments are also described.

### Sample Preparation

Zirconium alloy (Zircaloy-4) samples, with chemical composition given in Table 3.1, were used as substrate. Generally these alloys are rolled at high temperature in the beta region, then solution treated at about 1065°C (1950 F) and water quenched. Subsequent hot working and heat treating is done in the alpha region (below 790°C) to preserve the fine, uniform distribution of intermetallic compounds that result from solution treating and quenching. The samples were cut by EDM (Electric Discharge Machine) to 5/8-inch diameter x 1 mm thick disks. Four groups of Zircaloy-4 samples were prepared, coated and characterized during the project time.

Table 3.1 Chemical composition of Zircaloy-4.

Sn	Fe	Cr	Si	C	O	Zr
1.37	0.2	0.11	0.01	0.014	0.124	Bal.

The first group of Zircaloy-samples (Group A) consists of 12 round samples which were prepared to study the film thickness effect on the adhesion and quality of SiC coating. Samples were ground to 600 grit and ultrasonically cleaned in water before they were sent for coating.

The second group of samples (Group B) was developed to study the effect of substrate surface preparations on the coating quality. The group consists of 35 Zircaloy-4 round samples with a 5/8" diameter and were prepared with 7 different conditions (5 samples for each condition) as follows:

1. As-Received
2. 600 Grit grinding
3. 240 Grit grinding
4. Pickled
5. Grit blasted
6. Pre-Oxidized
7. DLC coating

The grinding of thin Zircaloy specimens was carried out by placing the sample on aluminum holder using thermal glue. The grinding started with the coarse grit size 240 and ended with the desired grit size using silicon carbide papers. After grinding, the holder was placed on the heater to dissolve the glue and release the sample. Ultrasonic cleaning in water for about 5 minutes was used after each grinding step and after releasing the sample from the holder.

The samples for pickling were first ground to 240 grit and ultrasonically cleaned. Pickling was performed using 25-50% Nitric Acid (70%Vol), 2-5% Hydrofluoric Acid (49%Vol) and water.

Grit blasting of the as-received Zircaloy samples used glass beads that roughened the surface to about 40-60 equivalent grit size and then cleaned ultrasonically in water for 5 minutes.

Pre-oxidation after grinding used the samples ground to 600 grit and then cleaned ultrasonically in water for 5 minutes. The samples were placed in a box furnace at 1200°C for 10 minutes and air cooled.

A diamond like coating (DLC) was applied to 5 samples which were ground to 600 grit. The DLC coatings were applied by Los Alamos National Laboratory (New Mexico) starting with surface clean using Argon and  $C_2F_6$ , followed by implantation with Si (silane) ( $Ar+SiH_4$ ) and finally deposited with ( $C_2H_2$ ) with total film thickness of 8780 Å. Another 5 samples were later prepared by a carbon sputtering process with 50-200Å thickness (polished to 600 grit and ultrasonically cleaned in water for 5 minutes before carbon coating).

The third group of Zircaloy samples (Group C) consisted of 12 round specimens which were prepared for coating with a different precursor. Samples were polished to 600 grit and ultrasonically cleaned in water for 5 minutes before they were sent for coating.

The fourth group of Zircaloy samples (Group D) consisted of 9 flat dog bone strips for tensile testing. The strips were 0.063in thick x 0.25in wide x 1.025in gauge length. The samples were ground on both sides to 600 grit and cleaned ultrasonically in water for 5 minutes and sent for coating. Three additional dog bone specimens were also prepared in the same way for ion implantation.

For scanning electron microscope (SEM) cross section characterization and film thickness measurements, coated samples were mounted using bakelite followed by grinding with SiC papers starting from coarse 240 grit up to fine 800 grit, polished to 0.3  $\mu\text{m}$  using alumina suspension and ultrasonically cleaned for 5 minutes in water. Etching was performed using a mixture of 1ml HF, 4.5 HNO<sub>3</sub> and 4.5 ml H<sub>2</sub>O for 10 seconds. A thin conductive Au film was sputtered on the surface to avoid charging effects in the SEM when high resolution images were required. However, when elemental analysis by EDS was required, carbon coating was used, because Au is a heavy material which will reduce detection of other element in the sample. The cross section was examined in the scanning electron microscope and the coating thickness was measured from at least 5 different areas on each sample.

### **Silicon Carbide Coating**

The silicon carbide coatings were prepared by a proprietary low temperature DC-pulsed plasma enhanced chemical vapor deposition (PE-CVD) technique developed by MER (Materials and Electrochemical Research Corporation, Tucson, Arizona). The



temperature of the substrate during deposition was approximately 360-375°C. Different precursors and film thicknesses were used in these coatings with 10-20% variation in film thickness..

The first group of Zircaloy (Group A) samples was coated using a (Si-Cl-C-H) precursor with two different film thicknesses. Six samples were coated with approximately 1 µm thick films and the other six samples were coated with approximately 5 µm thick films.

The second group (Group B), which consisted of 35 samples of different substrate preparations, was coated with 1 µm thick SiC films using the same (Si-Cl-C-H) precursor.

The third group of samples (Group C), which was used to study the effect of chlorine on the stability of SiC coatings, was coated using a trimethylsilane precursor with two different thicknesses. Three samples were coated with approximately 1.5 µm thick film and the other three with approximately 3 µm. Dog bone samples (Group D) were coated by 1.5 µm thick films from both sides using the same precursor.

Table 3.2 lists all sample preparation and coatings for all the groups of samples which were used in the experimental work.

### **Thermal Stability Test**

In order to study the effect of temperature on the adhesion and stability of SiC coatings on Zircaloy samples, thermal stability test was used.

Seven samples of Zircaloy-4 with different substrate conditions from the group B were used in this study. To avoid any interaction with the atmosphere, the samples were encapsulated under vacuum using Argon gas as shown in Figure 3.1. In order to avoid

explosion or shrinkage of the tubes at high temperature, the pressure inside the tube was set at 60 KPa at room temperature. This pressure translates to approximately 1 atmosphere at the heat treatment temperature.

Table 3.2 Sample preparation and coating procedure for all the groups.

Group	Major Purpose	No. of samples	Substrate roughness	Substrate Condition	Film Thickness, $\mu\text{m}$	Precursor
A	Thickness Effect	6	600 grit		1	Si-Cl-C-H
		6	600 grit		5	
B	Substrate Preparation effect	5	As-received		1	
		5	600 grit		1	
		5	240 grit		1	
		5	240 grit	Pickled	1	
			40-60 grit	Grit- blasted		
		5	600 grit	Pre-oxidized	1	
		5	600 grit	Carbon coated		
C	Chlorine effect	3	600 grit		1.5	Trimethylsilane
		3	600 grit		3	
D	Tensile tests (dog bone specimens)	3	600 grit		1.5	
		3	600 grit		1.5	
		3	600 grit	Pre-oxidized	1.5	
	Implantation effect	3	600 grit	Implanted with Hydrocarbons	-	No coating

The encapsulated samples were put into a box furnace at 350 °C for 500 hrs and then air cooled. Samples were taken out from the capsule and analyzed by SEM and energy dispersive spectroscopy (EDS). Scratch tests utilized two samples (600 grit and 240 grit substrate surface finish).



Figure 3.1 Seven zircaloy-4 samples coated with SiC are encapsulated before they placed in box furnace for thermal treatment.

### **Hydrothermal Autoclave Test**

The autoclave is a high pressure, high temperature system used to simulate the conditions experienced by Zircaloy cladding inside a light water reactor. The autoclave system used in the experiments, shown in Figure 3.2, basically consists of a high pressure vessel made of 316 SS, electric resistance heater, seal system, pressure regulator, safety head valve to control the pressure and thermocouple for temperature control. The sample holder is made of stainless steel and can hold up to 7 samples. The maximum allowable pressure is 6000 psi.

The hydrothermal effects on SiC coatings were examined in the autoclave under static condition in 3000psi de-ionized water at 350°C for 24 hrs. Seven samples having different substrate preparations from group B were tested in the autoclave. Other test included two samples from group C which had different film thicknesses and were coated using a trimethylsilane precursor.

The samples were placed in a stainless steel jig that can hold up to 7 samples. When the exposure was complete, the samples were removed after cooling down to room temperature and dried in air. Samples were weighed before and after exposure to determine the weight loss/gain. SEM and EDS analysis were made for all samples.

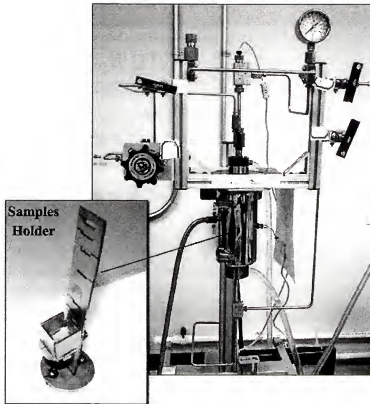


Figure 3.2 The autoclave system used for hydrothermal testing of SiC coatings (manufactured by Autoclave Engineers).

### **Characterization of Coatings**

Different analytical techniques were used to quantify and qualify the mechanical, chemical and topographical properties of SiC coatings, the adhesion between film and substrate and the corrosion and thermal resistance of the coatings.

### **SEM/ EDS**

Scanning electron microscopy (SEM) was used to measure the thickness of the films and to study their structure and morphology at magnification up to 30,000X. The analysis utilized a JEOL JSM 6400 SEM and was operated typically at 15 KeV at working distance of 15 mm with both backscattered and secondary electrons modes of operation. Secondary electron mode was used to provide information about surface morphology while backscattered mode provides images based on the atomic number of

the different elements in the sample. The SEM system is also equipped with electron dispersive spectroscopy (EDS) which was used for quantitative elemental analysis. Mapping, line scan and quantitative analysis were also utilized to characterize the chemical composition of coatings before and after thermal and hydrothermal exposures. When insulating bakelite material was used for mounting samples for cross section studies, a thin conductive Au film was sputtered on the surface to avoid charging effects when high resolution images were required. However, when elemental analysis by EDS was required, carbon coating was used, because Au is a heavy material which will reduce detection of other element in the sample.

The scratch track morphology and modes of failure in scratch tests were also analyzed by SEM. EDS and backscattered imaging in the SEM were used to check the film failure, whether adhesive or cohesive, in scratch tests.

### **Roughness Measurements**

In order to quantify the surface roughness effects, profilometry measurements were made on samples before and after coating using a Wyko NT1000 profilometer. The profilometer is a non-contact technique which provided surface details in 2 and 3-D and surface roughness measurements from 0.1 nm to 1 mm. At least five tests were made from different areas on each sample and the average roughness was obtained.

### **Scratch Test**

The scratch test has long been used to assess the adhesion of thin hard coatings and is a useful tool for coating development and quality assurance. A Hysitron nanoindenter machine located in ERC-UF which has the ability to do nano-scratch testing of thin coatings by lateral movement of the tip was considered for adhesion tests in this project. However, after intensive training and preparation of the machine, it could not be used for

scratch tests of SiC coatings due to limitation in maximum normal forces required to scratch hard coatings. The maximum normal load in this machine is 5000  $\mu\text{N}$ . When micro scratch tester was used later, the first delamination occurred at 0.5 N load, i.e. 100 times the maximum load available with the nano scratch machine at the ERC-UF.

Consequently, a micro scratch tester (MST) at Micro-photonics (California) was used. Scratch-tests were done by generating 3-5 scratches on each coated sample using a spherical Rockwell C diamond stylus with a tip radius of 20 and 200  $\mu\text{m}$ . The stylus was drawn at a constant speed across the coating surfaces. The test parameters, which have been used for different groups, are shown in Table 3.3. The critical load was determined by a tangential force recording which enables the force fluctuations along the scratch to be followed and also by acoustic emission (AE) detection of elastic waves generated as a result of formation and propagation of microcracks.

Table 3.3 Test conditions for scratch analysis of samples from group A.

Parameter	Group A	Group B
Loading range	0 to 3 N	0 to 15 N
Loading rate, $dL/dt$	3 N/min	15 N/min
Scratch Length	5 mm	3 mm
Scratching speed, $dx/dt$	5 mm/min	3 mm/min
AE sensitivity, SAE	9	9
Indenter	20 $\mu\text{m}$	200 $\mu\text{m}$
Diamond reference number	C-020	L-205

### Indentation Test

The hardness and modulus of elasticity of the SiC film was determined by the Hysitron nanoindentation machine using a Berkovich tip. Microindentations of the substrate and film were also done using a Vickers microhardness tester with 500 gm and 1 Kg loads. The Vickers hardness number is obtained by dividing the indentation load by the surface area of the permanent indent made by a standard diamond indenter.

Hardness tests were also applied to the Zircaloy samples after ion implantation to measure the change in the hardness throughout the thickness. An indentation test using the Vickers's microhardness machine was made on the cross section of dog bones cut by electro-discharge machine followed by polishing to  $0.3\ \mu\text{m}$  and ultrasonically cleaned. The indentation tests were made at  $0.15\ \mu\text{m}$  distance between each two indents as shown in Figure 3.3 The Rockwell (HRA 60kg) hardness test was also made for treated and untreated Zircaloy-4.

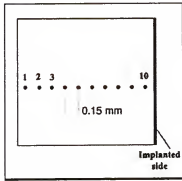


Figure 3.3 Cross section of implanted Zircaloy sample shows the location of indentation tests.

### X-ray Diffraction Analysis

X-ray Diffraction (XRD) is a powerful technique used to identify crystalline phases present in materials and to measure the structural properties (strain state, grain size, phase composition and defect structure). The advanced X-ray machine (X'Pert) was used to determine the crystallinity of the SiC coatings and for residual stresses measurement. Residual stresses can be determined by XRD which has the high accuracy enough to detect small shifts of the lattices constants due to strains.

Because the surface layer is very thin, grazing angle x-ray diffraction (GIXD), which can penetrate only several hundred angstroms from the sample surface, was performed at low incidence angles of  $0.5^\circ$  and  $1^\circ$ . X-ray analysis was made for the top

surface of the one of the samples from group B. It was also made for as-received Zircaloy sample for comparison with the coated sample.

### **Tensile Tests**

Tensile tests were made at room temperature using an INSTRON Servohydraulic tensile machine equipped with an extensometer to ensure high accuracy measurements in the low strain range. Tests were performed at a constant crosshead speed of 0.1 in/min and the test was paused at 2%, with a suspension of the data capture to remove the extensometer and resumed the test. The machine is provided with computer software (Merlin) for online recording and collection of data and generation of the stress-strain curves. Tests were made for coated samples, to check if there is any effect from coatings on the mechanical properties of the Zircaloy material. The same test was also carried out for non-coated Zircaloy samples which have been implanted with hydrocarbons to check the effect of ion implantation on the mechanical properties of Zircaloy.

Tensile tests were also used to determine the ultimate shear strength of a SiC/Zircaloy-4 interface by the periodic cracking method described in Chapter 1. As the metal is plastically stretched, the ceramic film develops cracks that are oriented transverse to the pulling direction. The density of the cracks (the number per unit length) increases as the amount of plastic strain in the metal substrate was increased. Eventually, the crack density reaches a constant value and is not influenced by further plastic deformation of the metal. The ultimate shear strength of the metal-ceramic interface is related to the tensile fracture strength of the ceramic film and the largest spacing between the cracks; both of these quantities are measured in this technique.

The specimens were pulled uniaxially in an INSTRON tensile machine equipped with an extensometer to get high accuracy measurements in the low strain range. Tensile



tests were paused at different specific levels of strains, as shown in Figure 3.4 to measure the crack spacings and tensile-strain curves were generated.

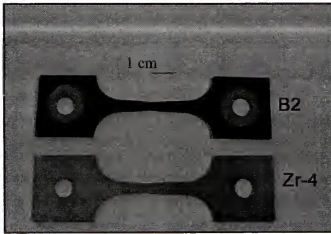


Figure 3.4 Two dog-bone samples. Tensile test paused at 30% strain. B2: Zircaloy-4 Coated with 1.5 $\mu$ m thick SiC film. Zr-4: Zircaloy specimen with no coating.

The samples were then examined in a scanning electron microscope to observe and measure the developments of cracks in the SiC film after each test. Strains of 1%, 2%, 10% and 30% were used for this study. Because of the large size of samples, it was not possible to insert the samples in the SEM using the normal sample holder and the chamber was opened, after vacuum release, to fix the sample manually inside the chamber as shown in Figure 3.5.

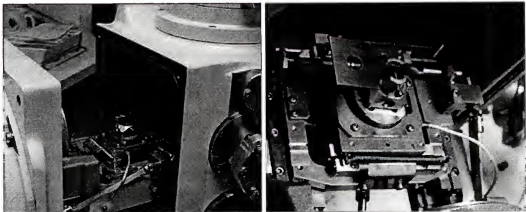


Figure 3.5 Dog bone samples were fixed manually in the SEM for cracks characterization.

## CHAPTER 4

### RESULTS

The results of this study are organized in the following manner, (1) x-ray characterization of SiC coatings, (2) effect of the SiC film thickness on the coating quality, (3) effect of substrate preparation on the adhesion, (4) thermal stability of SiC coatings, (5) hydrothermal tests of SiC coatings, (6) characterization of "Trimethylsilane" coatings (7) effect of ion implantation on the mechanical properties of Zircaloy-4, (8) ultimate shear strength of the SiC/Zircaloy-4 interface, and (9) work of adhesion of the SiC films.

#### **X-ray Investigation of SiC Films**

Grazing angle x-ray diffraction (GIXD) was performed at very small incidence angles. However, because the surface layer was very thin, 1  $\mu\text{m}$ , the x-ray easily penetrates to the substrate material even at such a low angle. This explains the presence of Zr peaks in the GIXD patterns. The x-ray diffraction for coated and un-coated samples is shown in Figure 4.1(a). Almost all peaks that appeared can be identified as belonging to Zr and there are no peaks belonging to SiC as shown in Figure 4.1(b). Two strong peaks which don't correspond to Zr or SiC, located at  $\sim 30^\circ$  and  $\sim 50^\circ$  were attributed to  $\text{ZrO}_2$ , Figure 4.1(c), a surface oxide formed probably during handling or deposition.

Since, from these results, the SiC layer was found to be amorphous; it was not possible to determine the level of stress present in the film by x-ray diffraction techniques.

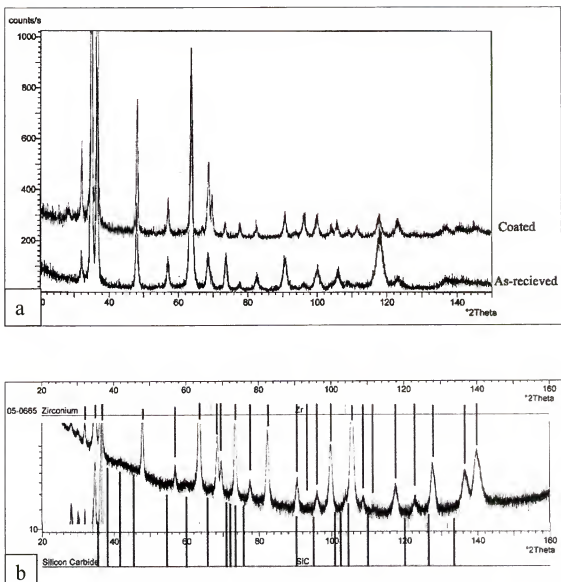


Figure 4.1 X-ray diffraction results for (a) coated and uncoated samples, (b) coated samples showing the corresponding peaks for zirconium and silicon carbide, (c) peaks correspond to zirconia.

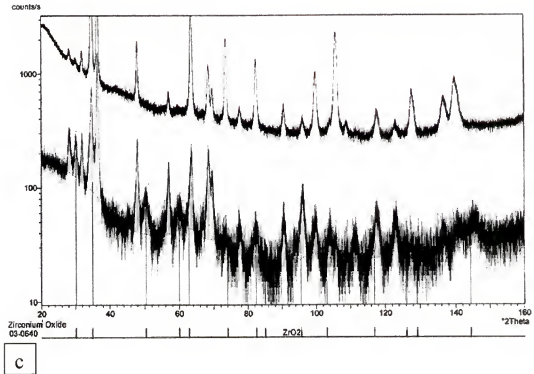


Figure 4.1 Continued.

### Film Thickness Effects

Two different SiC film thicknesses ( $1\mu\text{m}$  and  $5\mu\text{m}$ ) from group A were examined by SEM. The top surface and cross section of each sample were characterized. Figures 4.2(a and b) shows the surface morphologies of the  $5\mu\text{m}$  SiC film deposited on Zircaloy-4. Many cracks can be seen on the surface of SiC, similar in appearance to cracks that form in dried mud. Figures 4.2 (c-f) show the cross-sectional SEM image of the deposited films near the interface. Cracks propagated through the film but no cracks were observed to continue into the Zircaloy-4 substrate. Some cracks turn away before they reach the interface, Figure 4.2(e) and some of them propagate through the interface , Figure 4.2 (f).

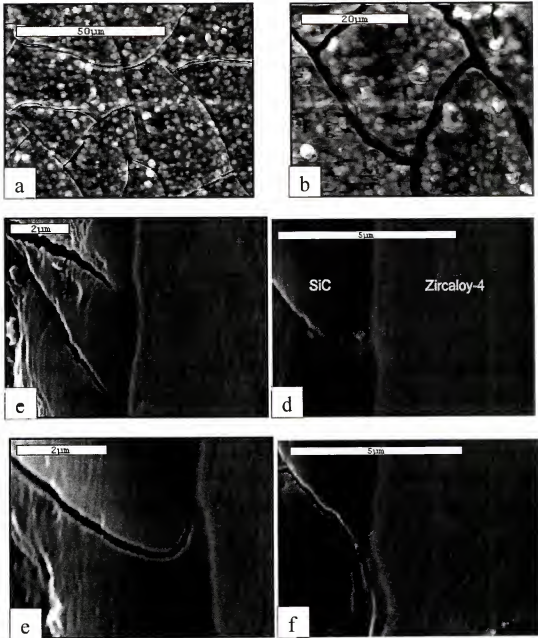


Figure 4.2 SEM images of SiC films of 5μm thickness deposited on Zircaloy-4 substrate (a,b) top surface shows a "mud" pattern of the cracks, (c-f) cross section show the propagation of cracks through SiC film.

When 1μm thick SiC films were examined, no cracks were observed on the coating surface. The top surface of the SiC film is shown in Figure 4.3(a and b). There are features on the surface that are parallel and were thought to be the result of polishing scratches before coating. These features were not observed on the 5μm SiC coatings due

to the much greater coating thickness. Figure 4.3(c and d) shows the cross-sectional SEM analysis of the  $1\mu\text{m}$  deposited films near the interface. The coating film is very flat and smooth and there are no cracks or voids apparent in the film or the interface.

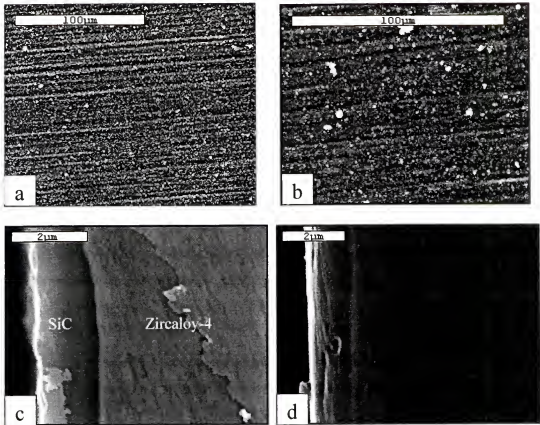


Figure 4.3 SEM images of SiC films of  $1\mu\text{m}$  thickness deposited on Zircaloy-4 substrate (a, b) top surface, (c, d) cross section.

A scratch test was made on the samples of different film thicknesses. The average critical load was obtained by generating 3 scratches, 5mm long, for each sample as shown in Figure 4.4. During testing, the applied normal force, the tangential force and the acoustic emission AE signal intensity were recorded. Figure 4.5(a) shows a typical graph obtained from one of the scratch tests. The critical load is taken at the point where there is a change in the friction between stylus and surface. Figure 4.5(b) shows good agreement between the results from tangential force measurements and acoustic emission detection

in the determination of critical load. Greater loads were required to cause delamination in thick SiC films than for a thin film as shown in the results in Figure 4.6.

The scratch tracks, as examined by SEM, were composed of three stages with an increase in the applied loads. The first stage, at low applied load, involved plastic deformation of film and substrate, which caused some flaking of the film around the scratch line. The second stage indicated the appearance of cracks and detachment of small pieces ahead of the scratch stylus. The third stage, which starts at the critical load, contains continued delamination of the film ahead of the scratch stylus. SEM was also used to determine the type of failure, whether cohesive failure within the coating or an adhesive failure at the interface of the coating-substrate system. Figure 4.7 shows the SEM images for the first delamination in the thin film (Figure 4.7(a)) and the continuous delamination in thick film, Figure 4.7(b). The film delamination was due to an adhesive failure since the backscattered images indicate no SiC present in the delaminated region.

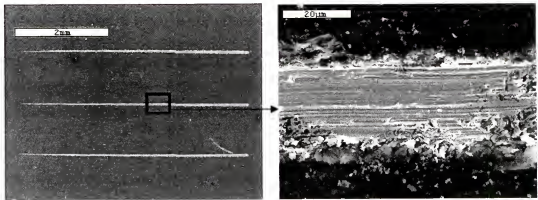


Figure 4.4 SEM micrographs of the scratch channels on the 1  $\mu\text{m}$  SiC film on Zircaloy-4.

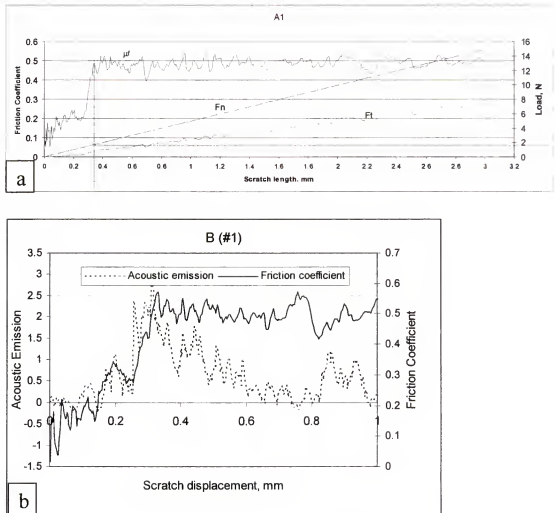


Figure 4.5 Typical graphs of scratch test show (a) variation of normal force and tangential force as function of scratch length, (b) good agreement between friction measurement and acoustic emission detection in the scratch test.



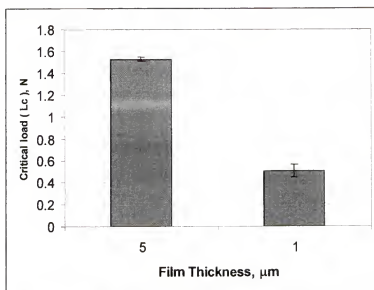


Figure 4.6 Critical load as function of film thickness obtained from scratch test.

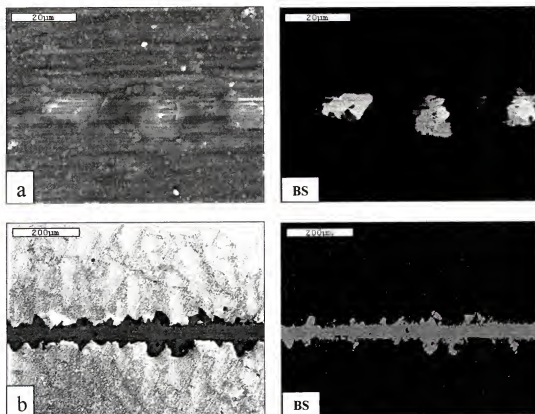


Figure 4.7 SEM secondary electron and backscattered (BS) micrographs shows the morphology of coating failure due in scratch test (a) first delamination in the  $1\mu\text{m}$  SiC film, (b) continuous delamination in the  $5\mu\text{m}$  SiC film.

### **Substrate Surface Preparation Effects**

Silicon carbide coatings on Zircaloy substrates with different preparations, including different roughness levels, pickling, pre-oxidation and use of intermediate layer, were characterized by profilometer, scratch testing, nano-indentation, SEM and EDS techniques.

The surface roughness test for the samples surface before and after coating was made by Profilometry. Different mathematical values of roughness and the 3D imaging, as shown in Figure 4.8, were obtained for each test. Roughness results for all samples of Group B are summarized in Table 4.1. The value,  $R_a$ , is the arithmetic mean roughness value, which is the average value of all absolute vertical distances of the roughness profile from the center line within the measuring length.

The surface roughness after coating does not necessarily represent the roughness before coating. For example, the Surface roughness decreased to almost the half value after coating for the 240 grit surfaces, but increases for the 600 grit samples and for the as-received surfaces. These large differences of roughness before and after coating mean that the conformality of the coating was not very high and the thickness of the film at peaks and valleys is different. Roughness of the pre-oxidized sample has also increased to the twice of its original value (600 grit) after oxidation and coating. However this increase could be attributed to the rough and thick oxide layer.

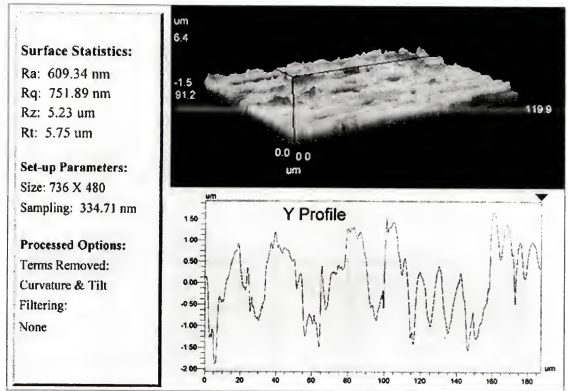


Figure 4.8 Typical profilometer measurement of roughness showing roughness data, 3D image and y-profile.

Table 4.1 Roughness of all samples surfaces of Group B before and after coating.

Sample	Roughness, Ra, nm	
	Substrate	After Coating (1μm)
A-As-received	224	342
B-600 grit	307	377
C- 240 grit	945	500
D- 240 grit and pickled	945	593
E -Grit blasted	2518	2315
F-Pre-oxidized	307	720
H-carbon interlayer	307	473

Secondary and backscattered electron SEM images were obtained for all coated samples. The secondary electron SEM imaging indicates topographical features as scratches or cracks. Backscattered electron SEM images will identify compositional differences, particularly if cracks propagate to the base metal are present. Since the film is very thin, the coating surface reflects the morphology of the substrate. Although

significant scratches were seen (Figure 4.9) on all coating surfaces, which were caused by grinding the substrate before coating, the backscattered images do not show a similar morphology. Therefore, these scratches do not reach the substrate.

In the as-received substrate, the scratches on the surface of the film were non-uniform (Figure 4.10(a)) because the substrate was not polished prior to coating. The film on grit-blasted Zircaloy-4 exhibited different morphology, as shown in Figure 4.10(b), due to the irregular surface left on the Zircaloy-4 sample due to the blasting of the substrate with glass beads particles.

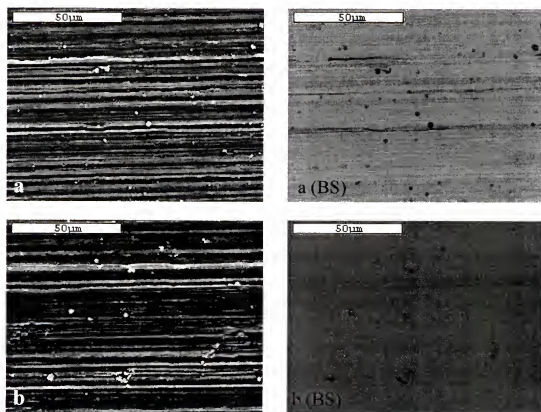


Figure 4.9 Typical secondary electrons and backscattered (BS) images of a coated surface on (a) and (b) 600 grit polished substrate, (c) and (d) 240 grit polished substrate.

The only sample which exhibited any evidence of cracks in the SiC film surfaces, was the pre-oxidized substrate sample as shown in Figure 4.11(a,b,c). These cracks

appeared to form due to cracks and spallation of the approximately 100  $\mu\text{m}$  thick brittle oxide film formed on the Zircaloy substrate during the pre-oxidation treatment. The cross section SEM images of oxide/substrate interface are shown in Figure 4.11(d,e,f). The thick oxide layer was formed due to oxidation temperature, 1200°C, which leads to the formation of  $\text{ZrO}_2$ . No cracks were observed to propagate through the oxide layer, and most of the cracks were found along the interface as shown in Figure 4.11(d). However, some cracks were found to propagate in a region between the oxide film and Zircaloy metal (Figure 4.11 (e-f)) which could be caused by an embrittlement of the zirconium metal by oxygen.

The high temperature oxidation was chosen to produce a dense tetragonal structure of zirconia. Figure 4.12 shows the microstructure of zirconia formed at 1200° which consists of equiaxed grains with an average grain size of 1-2  $\mu\text{m}$ . The microstructure has the same appearance of the tetragonal zirconia (t- $\text{ZrO}_2$ ) found in the literature [91, 92].

However, when lower oxidation temperature were used, only thin oxide layers, 0.25 $\mu\text{m}$  (Figure 4.13(a)) and 4 $\mu\text{m}$  (Figure 4.13 (b)) films were formed at 500°C , and 750°C respectively. Therefore, it is recommended for any future work to pre-oxidize the Zircaloy at some temperature below 500°C to get a thin oxide layer with no cracks.

All coated samples regardless of film thickness or surface preparation show similar EDS profile as shown in Figure 4.14. Chlorine peaks were found in all samples and is thought that this may be detrimental to the corrosion resistance of SiC films [93].

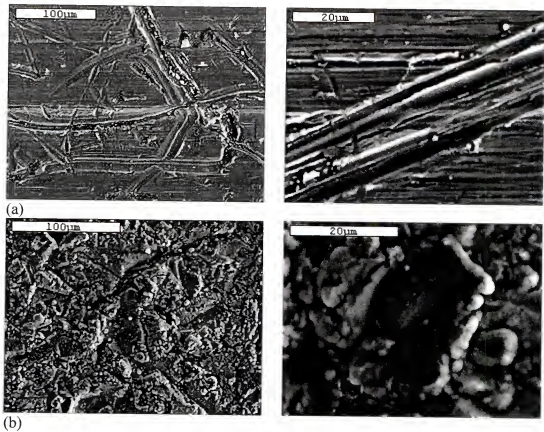


Figure 4.10 Low and high magnification SEM image of the top surface of the SiC films (a) deposited on the as-received Zircaloy-4 sample, (b) deposited on grit blasted (high roughness) Zircaloy-4 substrate sample.

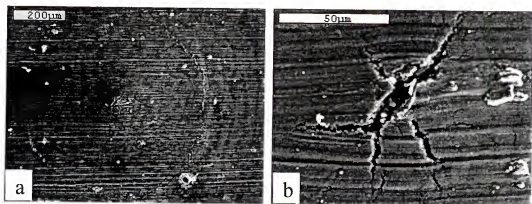


Figure 4.11 SEM images show the thickness and cracks on the oxide film of zircaloy-4 oxidized at 1200°C (a,b,c) top surface, (d,e,f) cross section.

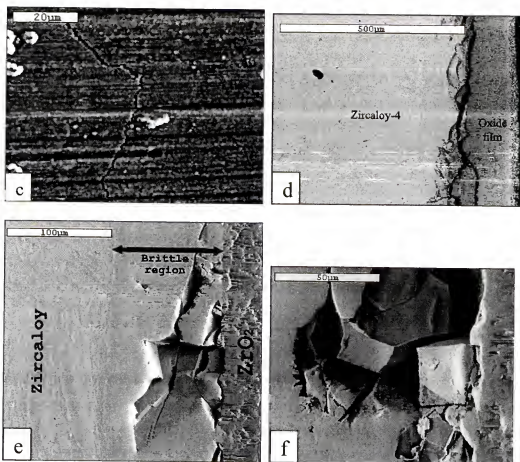


Figure 4.11 Continued.

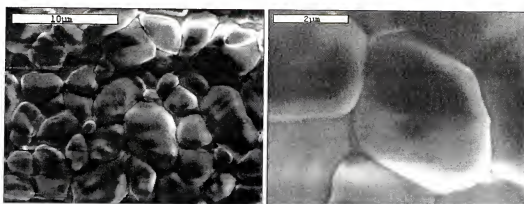


Figure 4.12 SEM images show the appearance of zirconia when Zircaloy exposed to 1200°C for 10 min in dry air.

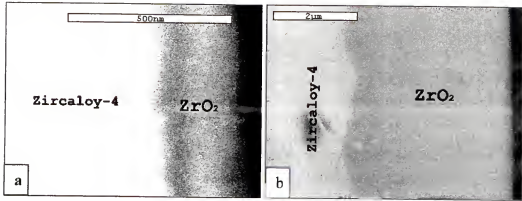


Figure 4.13 SEM images for the cross section of oxidized Zircaloy-4 in dry air at (a) 500°C, (b) 750°C.

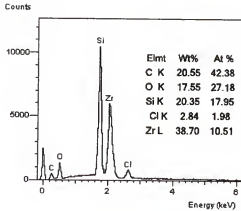


Figure 4.14 Typical EDS spectrum of top surface of Zircaloy-4 coated with 1 µm thick SiC film of group B samples.

Scratch tests were performed on seven coated samples of group B that had different substrate surface preparation. Three to five scratches, approximately 3mm long, were made for each sample as shown in Figure 4.15. The test conditions for the evaluation of these samples are given in Table 3.3. Adhesive failure was observed on all samples, as shown in back scattered SEM images and confirmed by EDS analysis of scratch channels, Figure 4.16. The critical force,  $L_c$ , for each samples at which damage of the coating occurs is given in Figure 4.17. The pre-oxidized sample did not show any clear delamination of the film up to loads approaching more than 30 N. The graph shows a



higher adhesion strength for 240 grit finish compared to the other finer and rougher surfaces (600 grit and the grit blasted samples) respectively. Figure 4.18 shows the variation of the critical load as a function of the coating surface roughness. Higher adhesion strengths were observed at a moderate level of substrate roughness. Coating on pickled substrate shows higher critical loads than when only ultrasonically cleaned. No data could be developed for samples with a DLC interlayer since no samples were available. The DLC samples were replaced by samples with a sputtered carbon interlayer which did not show any noticeable effect on the adhesion.

Figure 4.19 shows the morphology of scratch tracks on SiC film at the low load regime before the start of continuous delamination. Detachment and spallation of the film around the scratch tracks were observed. The coating was removed due to the plastic deformation of the film and/or substrate rather than direct contact with stylus. This type of delamination is a typical event for the adhesive mode of failure when the film tends to flake away or depond at the edges of scratch channel.

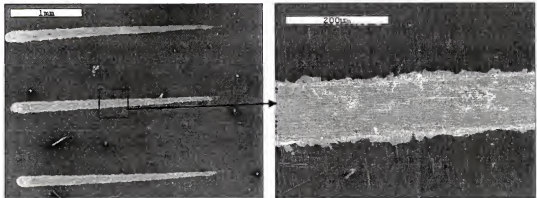


Figure 4.15 SEM micrographs of the scratch channels on the 1  $\mu\text{m}$  SiC film on Zircaloy.

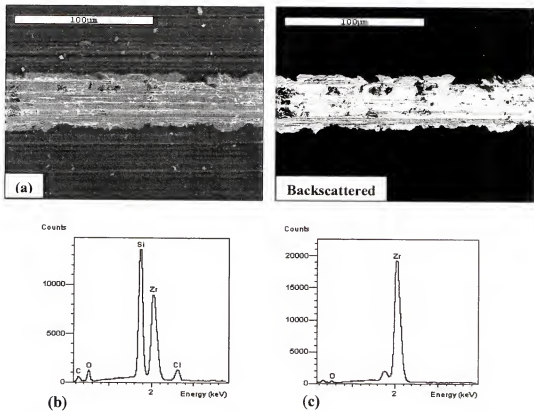


Figure 4.16 Coated sample after scratch test shows adhesive failure (a) SEM SE and BS images of scratch track, (b) EDS spectrum from coated area, (c) EDS spectrum inside scratch track.

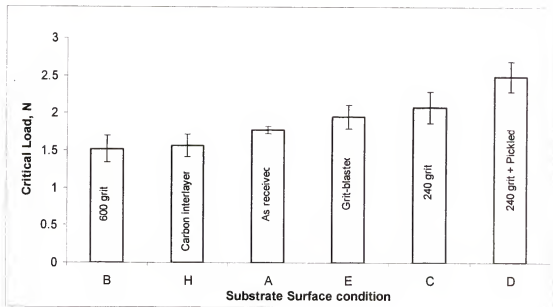


Figure 4.17 Critical load of SiC coating failure as a function of substrate surface preparation for samples of Group B.

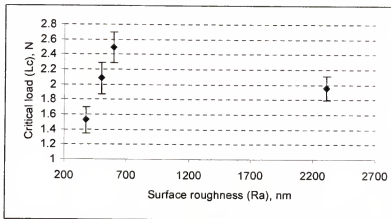


Figure 4.18 The variation of critical load with coating surface roughness.

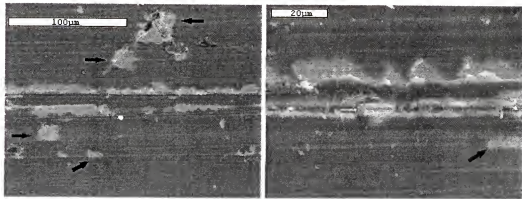


Figure 4.19 SEM images of SiC coatings show detachment of the film around the stylus track.

### Thermal Stability Tests

SEM and EDS characterization has shown (Figure 4.20) no change in the surface morphology and composition of the coating after heat treatment in vacuum at 350°C for 500 hrs.

A scratch test was made for two coated samples (600 grit and 240 grit polish substrates) of group B after heat treatment. Three scratches, approximately 3mm long, were made on each sample using test conditions given in Table 3.3. For each measurement, the acoustic emission (AE) signal, the tangential force ( $F_t$ ), and the penetration depth were recorded versus the normal forces ( $F_n$ ) as shown in Figure 4.21.

The critical force,  $L_c$ , at which damage of the coating occurred, was obtained. Results (Figure 4.22) showed much higher adhesion strength of the samples after heat treatment than for as-coated samples.

Figure 4.23 shows the difference in the morphology of scratch tracks of the heat-treated coatings and the as-coated samples. Although the same test conditions, such as normal load, load rate scratch length, were used in both tests, it can be observed that the continuous delamination in heat treated coatings did not start until higher normal loads were reached. The increased load required to cause delamination in heat treated coatings confirms the higher critical loads found in heat-treated samples.

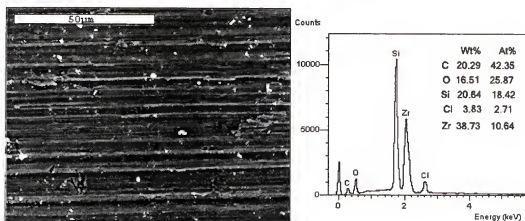


Figure 4.20 SiC coatings after heat treatment at 350°C for 500 hrs in vacuum (a) SEM image of the top surface, (b) EDS spectrum.

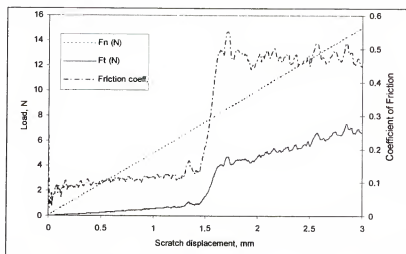


Figure 4.21 First scratch in the sample B2.

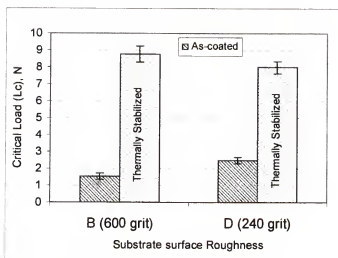


Figure 4.22 Critical load of the failure of the heat treated SiC coating compared to as-coated samples.

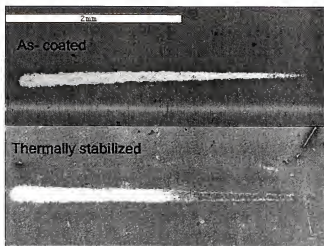


Figure 4.23 Scratch channel of as-coated and heat-treated samples.

### Hydrothermal Effects

Silicon carbide coatings were completely removed in autoclave testing when subjected to 350°C and 3000 psi for 24 hrs. The weight loss after exposure was significantly greater than weight loss of encapsulated heat-treated samples as shown in Figure 4.24. SEM and EDS characterization of samples after autoclave test have shown no SiC film on almost all samples. Only one sample (600 grit polish) was found to have partial failure in the film. This sample may have exhibited only partial failure due to its location in the autoclave. Figure 4.25 shows the sequence of a film failure in autoclave. Separations develop at the film/substrate interface as a result of tensions normal to the interface causes blistering and cracking Figure 4.25 (1-2). These separations start and develop preferentially parallel to the scratch lines and most probably along the asperities. Most of the buckles have an elliptical shape and propagates until they join the next buckle, Figure 4.25 (3). Complete spallation of the film occurs in some of the large buckles particularly those that contain previous cracks (Figure 4.25 (4-6))

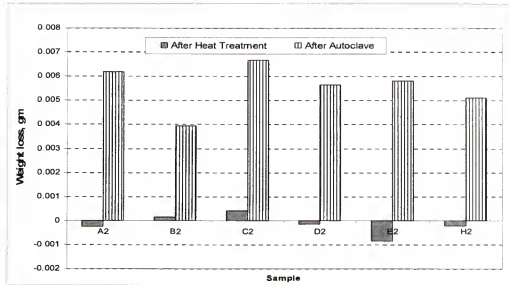


Figure 4.24 Weight loss of Zircaloy samples coated by  $1\mu\text{m}$  SiC film and exposed to thermal and hydrothermal conditions.

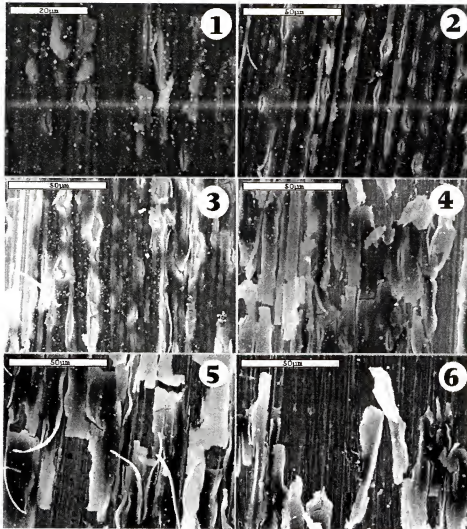


Figure 4.25 SEM images of SiC coating after autoclave, shows the sequence of failure (1) blistering and cracks, (2) propagation of buckles, (3 & 4) connection of adjacent buckles which lead to (5&6) complete spallation of the film.

#### **Characterization of "Trimethylsilane" Coatings**

The failure of SiC films in the autoclave testing was first believed to be caused by the presence of chlorine in the films which was an artifact from the precursor [93]. To determine the effect of chlorine in the previous coatings on the hydrothermal stability of SiC, six Zircaloy samples (Group C) were coated with SiC using trimethylsilane (TMS) as the precursor. Three samples were coated with approximately 1.5µm thick films. The other three samples were coated with approximately 3µm thick films.



SEM characterization shows some cracks on the 1.5 $\mu\text{m}$  film coatings, as shown in Figure 4.26(a). The 3 $\mu\text{m}$  thick films show better surface finish with no cracks or defects, as shown in Figure 4.26(b). The strong peak of Zr from the EDS spectrum, from samples with 1.5 $\mu\text{m}$  coating, shown in Figure 4.27, compared to that for 3 $\mu\text{m}$  could be attributed to the presence of cracks in the sample and the difference in film thickness.

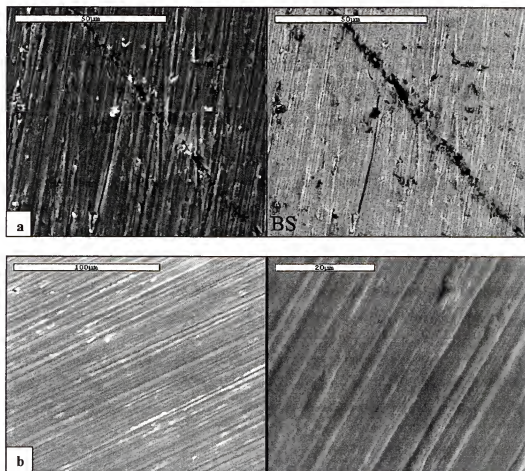


Figure 4.26 SEM images for (a) 1.5  $\mu\text{m}$  thick SiC, (b) 3  $\mu\text{m}$  thick SiC film on Zircaloy-4 substrate.

To determine the stability of the SiC coatings at hydrothermal conditions, samples of 1.5 $\mu\text{m}$  and 3 $\mu\text{m}$  film thickness were placed in an autoclave. The test conditions were the same as the previous test (350°C temperature and 3000 psi pressure for 24 hours).

Figure 4.28 shows the EDS analysis of SiC coatings after autoclave testing. No SiC coatings were observed or detected on any of the samples after autoclave testing. All of the peaks observed in the EDS correspond to Zr and oxygen.

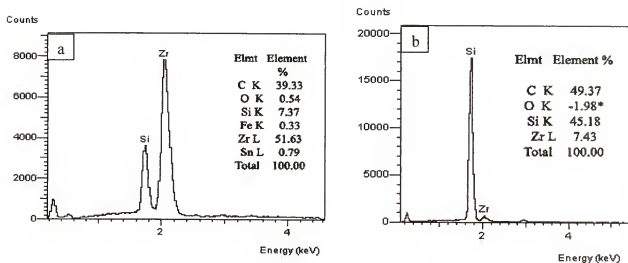


Figure 4.27 EDS spectrum for SiC films top surface with thickness (a) 1.5  $\mu\text{m}$ , (b) 3  $\mu\text{m}$ .

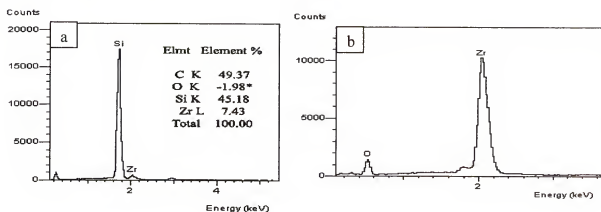
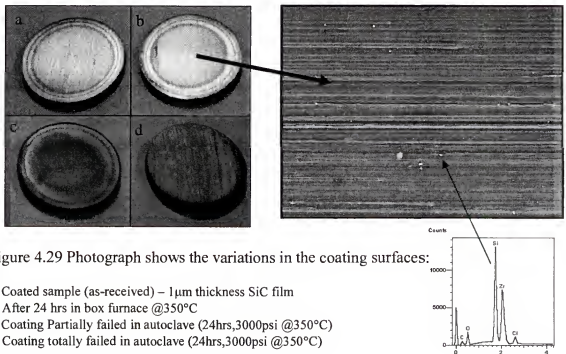


Figure 4.28 EDS for 3 micron thick SiC film on Zircaloy-4 substrate (a) before autoclave, (b) after autoclave testing.

### Thermal Stresses in Autoclave

One of the possible failure mechanisms of the SiC film in the autoclave was that the thermal stresses, which may be generated in the film during the cooling from test condition, caused cracking and failure of the film.

To determine the effect of thermal stresses on the SiC coatings in the dry air at the same temperature used in autoclave, coated samples from Group B were heat treated in dry laboratory air in a box furnace at 350°C for 24 hours. SEM and EDS results indicated no effect of the exposure on the film at these conditions. It can be seen from Figure 4.29 that the coating was not affected by thermal stresses compared to hydrothermal testing effects.



EDS was used to quantify the oxygen content of the same coatings (1 $\mu$ m SiC, Group B) after different exposure conditions as shown in Figure 4.30. Much higher contents of oxygen were found in the film after 24 hrs in the box furnace at 350°C compared to encapsulated samples exposed for 500 hrs at the same temperature. In fact, the oxygen content in the encapsulated heat-treated samples was almost the same as in the as-coated samples. However, the highest oxygen contents were found in the films after autoclave testing. The large scatter in the oxygen contents determined in autoclave

samples was attributed to the presence of cracks and delaminations in the films after autoclave test.

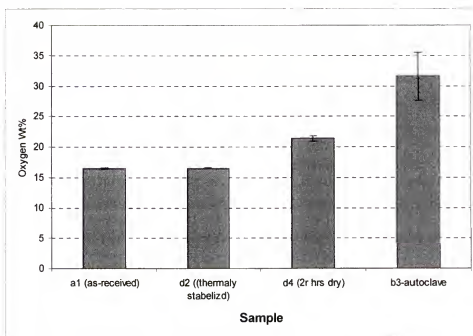


Figure 4.30 Oxygen content in SiC films after different thermal and hydrothermal treatments as analyzed by EDS.

### Ion Implantation Effects on Zircaloy-4

The effect of ion implantation on the mechanical properties of Zircaloy-4 was analyzed by tensile and indentation tests. Figure 4.31 shows the tensile test results for implanted and as-received Zircaloy-4 samples. It can be observed that the implanted samples had much lower ductility and higher tensile strength than the as-received samples. An increase of the hardness of implanted samples was also confirmed by Rockwell hardness (HRA 60kg) tests, as shown in Figure 4.32.

Figure 4.33 shows the microhardness data determined by Vickers microindentation testing through the cross section of implanted samples. It can be observed that the hardness increased as the implanted surface was approached, which confirms the

hardening effects of the ion implantation. Higher carbon content was found on the surface of the implanted sample as indicated by EDS and AES (Figure 4.34). Depth profile could not be performed by AES due to high roughness of the surface ( $> 1\mu\text{m}$ ) and very low sputtering rate ( $\sim 30\text{\AA}/\text{min}$ ).

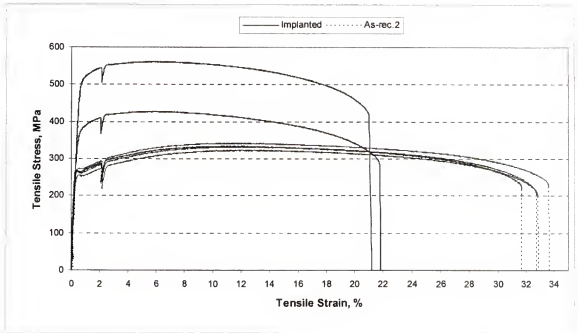


Figure 4.31 Stress-strain curve of Zircaloy-4 substrate with and without implantation.

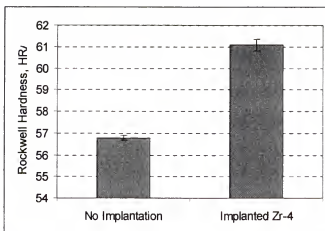


Figure 4.32 Rockwell (HRA 60kg) hardness of zircaloy-4 dog bones specimens with and without hydrocarbon implantation.

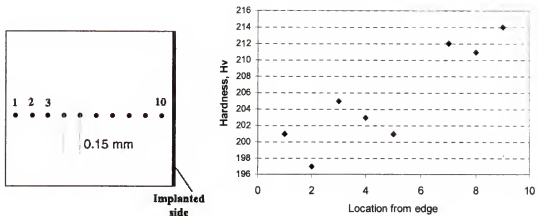


Figure 4.33 Vickers microindentation (Hv 1Kg) profile made to the cross section of the implanted Zircaloy-4 specimen.

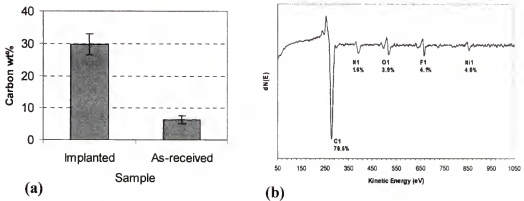


Figure 4.34 Carbon content in SiC film before and after implantation as analyzed by (a) EDS, (b) AES

### Ultimate Tensile Shear Strength

The ultimate tensile strength of the SiC coatings was measured by using the periodic cracking method, described in Chapter 2. The thickness of the SiC films, as measured by SEM, was approximately 1.4  $\mu\text{m}$  (Figure 4.35). The coated dog bone samples were pulled uniaxially in a tensile test machine and the test was paused at different strains (Figure 4.36). Samples were then examined in the SEM to characterize the coating. The SEM analysis showed that all cracks in the SiC films were formed normal to the tensile axis. Typical SEM photographs of the cracks in the SiC film at

different strains are shown in Figure 4.37. The distribution of the crack spacing in the SiC films at different strains is given in Figure 4.38.

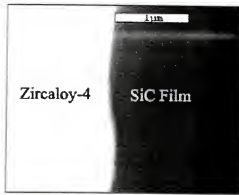


Figure 4.35 SiC Film thickness as measured by SEM.

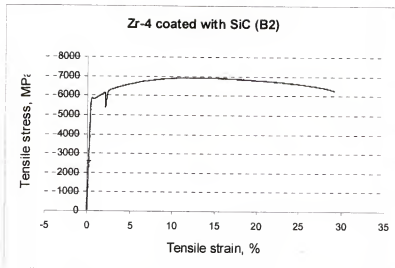


Figure 4.36 Tensile test of Zircaloy-4 coated with 1.5 micron SiC film. The test was paused at 30% strain to measure crack spacing.

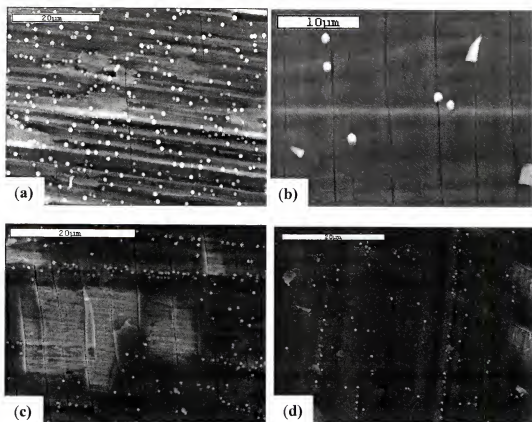


Figure 4.37 SEM micrographs of cracks caused by uniaxial tension at different strains (a) 0.5, (b) 2%, (c) 10%, (d) 30%.

Delamination and detachment of the SiC film was observed at 2% strain and higher (Figure 4.39), where parts of coating have disappeared due to delamination.

It can be seen from Figure 4.40, that the crack density in the SiC coating increased rapidly at  $\sim 2\%$  elongation. It will be assumed that the fracture strain of the SiC film was 2%, as used by Agrawal and Raj [74] in a similar approach. The crack density increased with increasing strain and reached a saturation value of  $\sim 230 \text{ mm}^{-1}$  at strains beyond 10%.



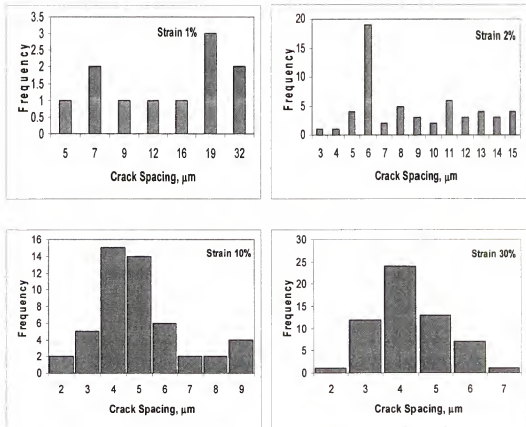


Figure 4.38 The distribution of crack spacing,  $\lambda$ , obtained at applied tensile strain of 1, 2, 10 and 30%.

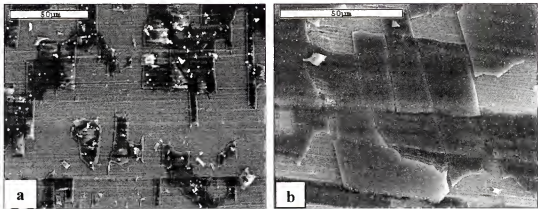


Figure 4.39 SEM micrograph shows detachment of SiC film at (a) 10% applied strain, (b) 2% applied strain.

The Young's Modulus was determined by a Nanoindentation experiment to be 115 GPa. The load-unload curve is shown in Figure 4.41. The maximum crack spacing, at a

constant crack density, is  $\lambda = 7 \mu\text{m}$ , as shown in Figure 4.34, at 30% strain. From these data, and by using Hook's law, equation (2.1), and assuming the film responded elastically, the fracture strength of the SiC film was :

$$\sigma_f = 2.3 \text{ GPa} \quad (4.1)$$

From equation (2.2) , the ultimate shear strength of the SiC/Zircaloy-4 substrate was calculated to be,

$$\tau_{\text{USS}} = 1.55 \text{ GPa} \quad (4.2)$$

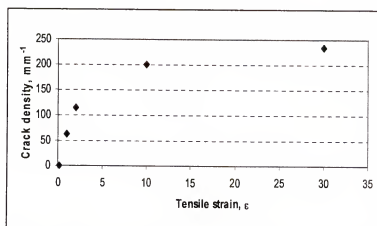


Figure 4.40 The variation of the crack density in the SiC film vs. applied strain.

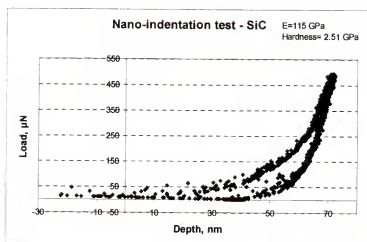


Figure 4.41 Loading and unloading curve of nano-indentation test on SiC film.

### Work of Adhesion

The practical work of adhesion values between SiC films and Zircaloy-4 was evaluated using two models from the literature which were presented in Chapter 2. Two coated samples from Group B having different surface preparation were used to evaluate the work of adhesion. In the first calculation, the Bull and Rickerby model [77] was used. The work of adhesion from Equation (2.5) is:

$$W_{AD} = \frac{32hL_c^2}{\pi^2 d^4 E} \quad (4.3)$$

The Second model, Laugeir [70], was applied by using Equation (2.3). In this model, the compressive stresses responsible for failure are a function of the applied stress  $\sigma_{appl.}$  and the internal residual stresses in the film  $\sigma_{int}$

$$\sigma(x) = \sigma_{appl.}(x) + \sigma_{int}(x) \quad (4.4)$$

From Equation (2.4) and for a Poisson's ratio of 0.37 for Zircaloy-4, the applied stress can be written as:

$$\sigma(x)_{appl.} = \frac{2P}{\pi d^2} (5.15f - 0.26) \quad (4.5)$$

Residual stresses in the film,  $\sigma_{int}$ , were estimated from the thermal expansion mismatch between the film and substrate, using [78] :

$$\sigma_{int} = E_f (\alpha_f - \alpha_s) \Delta T \quad (4.6)$$

The channel width of scratches,  $d$ , was measured from SEM images as shown in Figure 4.43. The radius of contact,  $a$ , is approximately equal to  $0.5d$  [76]. The critical load,  $L_c$ , and the coefficient of friction,  $f$ , were measured by scratch tests. The data used in the calculation and the results are shown in Table 4.2.

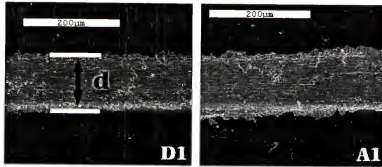


Figure 4.42 SEM images show the scratch channels for samples D1 and A1.

Table 4.2 Data and results for calculation of the work of adhesion for SiC coatings on the Zircaloy-4 substrate.

Sample	A1	D1
Substrate	As-received	240 grit
Poisson's ratio of Zircaloy-4 [4]	0.37	0.37
Coefficient of thermal expansion, Zr,	$5.7 \times 10^{-6}$	$5.7 \times 10^{-6}$
Coefficient of thermal expansion, SiC	$4.8 \times 10^{-6}$	$4.8 \times 10^{-6}$
Young's Modulus of SiC, $E_f$	212 GPa	212 GPa
Coefficient of friction, $f$	0.45	0.5
Film thickness	1 $\mu\text{m}$	1 $\mu\text{m}$
Residual stresses, GPa	0.064	0.064
Radius of contact, $a$	0.5d	0.5d
Critical load, $L_c$ , N	1.78	3.18
Channel width	101	92
$\sigma_{\text{appl}}$ , GPa	0.29	0.52
WAD (Bull and Rickerby), $\text{J/m}^2$	0.464	1.9
WAD (Laugier), $\text{J/m}^2$	0.2	0.8

## CHAPTER 5 DISCUSSION

### **Adhesion of SiC Coatings to Zircaloy Substrate**

The experimental results indicated that all SiC coatings used in this project, without exception, showed an adhesive failure when tested by scratch and indentation tests. Plastic deformation of the substrate due to compressive stresses induced by the scratch stylus caused flaking of the film from the substrate around the indenter, as shown in Figure 4.20, and confirmed by indentation test, Figure 5.1. It was reported [94] that in order for film to conform to substrate deformation; a limited ductility is required in the coatings. In the adhesive failure, the coating tends to debond or flake away at the edges of the groove particularly with brittle films. In a cohesive failure, there will be no flaking of the film but the indenter induces a shear which removes material only from the scratch channel.

The higher critical loads found in thick ( $5\mu\text{m}$ ) films in Group A compared to the thin ( $1\mu\text{m}$ ) films did not necessarily mean the coating exhibited higher adhesion. In the scratch test, the stress required for coating detachment is transmitted through the coating; therefore, thicker layers may require a greater surface stress to achieve the same shear at or near the interface, thus showing higher critical loads [56, 57, 95]. This result was found to agree with the literature reports [45, 53, 54, 94, 96], where the stress required for the cracking of thin brittle films on ductile substrates is related to the inverse of the coating thickness (see Figure 1.5). This is, however, one of the problems of the scratch

test technique when two coating systems with different coating and/or test parameters are compared.

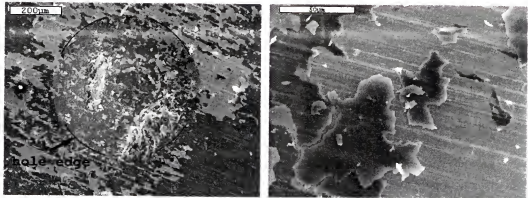


Figure 5.1 SEM images shows adhesive failure of the SiC films around indentation hole caused by plastic deformation of the substrate in indentation test using Rockwell (HRA 60kg).

Flaking of the film around and at the edges of scratch track at the low applied load stage was observed in thin films (Figure 4.20) and only at high loads for thick films (Figure 5.2). This difference could be attributed to the stresses which built up in the coating and could not extend to the substrate in the large thickness film until higher loads were applied and consequently, the energy was relaxed by cracking the film instead of deforming the substrate plastically [49]. The critical load values for SiC films in this study (1.5 -2.5 N) are lower than those found [49] in the literature (9-15 N) for SiC films deposited on steel substrates by PE-CVD which is attributed to high deposition temperature of 870°C.

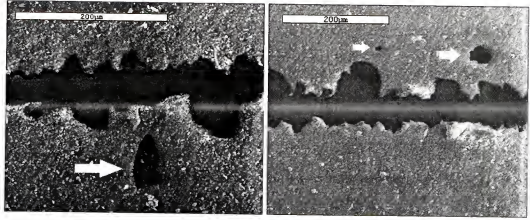


Figure 5.2 Two SEM images show flaking of the film around scratch channel on 5  $\mu\text{m}$  thick SiC film on Zircaloy substrate.

### Cracks in 5 $\mu\text{m}$ SiC Films

These cracks, as shown in Figure 4.2 (a), are similar in shape to the cracked developed in mud by shrinkage due to drying [97]. The mud crack pattern were also found in brittle thin films subjected to biaxial tensile stresses[98-102] (See Figure 5.3). Calcination of brittle films was also found to produce such pattern of cracks by tension due to excessive evaporation [103-105]. These cracks are also known as channel cracks, which could be formed by pre-existing flaws and elongates laterally in the film, as shown in Figure 5.4 until they meet a film edge or another cracks. It was found [99] that channel cracks will not form when the driving force is below the crack resistance of the film, i.e. when:

$$\beta \frac{(1-\nu^2)\sigma^2 h}{E_f} < \Gamma_f \quad (5.1)$$

where  $\nu$ ,  $h$ ,  $E_f$  are Poisson's ratio, thickness and toughness of the film,  $\beta$  is dimensionless number depends on the elastic constants of the film and the substrate, and  $\sigma$  is the tensile stress. This equation was derived from the edge crack in an infinite homogeneous material, when the crack size is comparable to the film thickness, where in this case, the

crack will propagate laterally in the film. It can be seen from Figure 5.5 that cracks in the thick SiC film have extended until they reach the substrate surface (these cross section SEM micrographs were produced after etching the Zircaloy).

As we can see from Equation 5.1 that increasing film thickness will increase the possibility for the formation of channel cracks and this may explain why these cracks did not form in the thin  $1\text{ }\mu\text{m}$  SiC coatings.

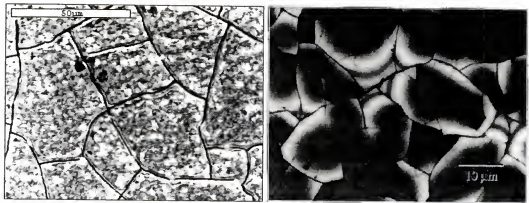


Figure 5.3 Plane view of channel "mud" cracks found in (a) SiC films of  $5\text{ }\mu\text{m}$  thickness on Zircaloy substrate in our work, (b) Silicon nitride film of  $1\text{ }\mu\text{m}$  thick reported on silicon substrates caused by tensile stresses [99].

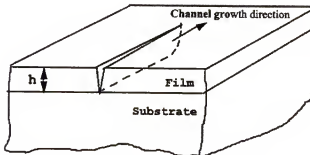


Figure 5.4 Growth of channel crack in the film.

However, this type "mud pattern" of cracks was found only to occur when film is subjected to the tensile stresses. The SiC films were expected to exhibit compressive residual stresses due to the lower thermal expansion coefficient based on the bulk



properties. The physical properties of thin films are often very different from those of bulk materials because of anisotropic atomic density distribution [106] and also because of defects [107]. For example, the coefficient of thermal expansion of Al was found to increase from  $18.23 \times 10^{-6} / ^\circ\text{C}$  to  $29.97 \times 10^{-6} / ^\circ\text{C}$  (i.e. 66% increase) when the film thickness increases from 0.3 to 1.7  $\mu\text{m}$  [107]. Compare this large change in CTE due to the thickness change to the small difference in CTE between Zircaloy and SiC,  $5.7 \times 10^{-6} / ^\circ\text{C}$  and  $4.8 \times 10^{-6} / ^\circ\text{C}$  respectively (only 18% difference). The increase in CTE value was attributed to the trapped impurities in the film which increase with increasing film thickness because the thermal expansion of a material is generated by the increase of the average interatomic distance during heating.

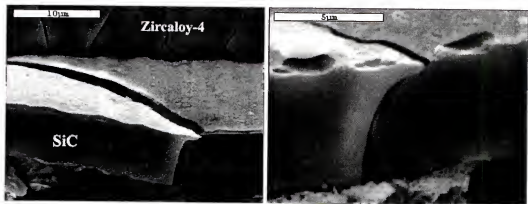


Figure 5.5 SEM images show a cross section of SiC film where channel cracks were found to reach the interface.

Thick films tend to develop higher residual stresses during deposition than thinner coatings [108] and since the SiC coatings were amorphous; some of the stresses associated with dislocations and grain boundaries do not contribute in the resistance of crack propagation in the film [109]. Furthermore, the amount of defects was found [57] to increase with increasing film thickness which may also act as crack initiation sites in the film.

### **Effect of Substrate Surface Treatment**

Substrate surface roughness was a very important factor in the adhesion of thin films to the substrates. The higher critical loads were found in intermediate values of substrate surface roughness. Scratch tests showed that a smooth substrate, 600 grit, polish induces a relatively poor adhesion strength compared to a rough 240 grit polish substrate, which was attributed to the larger contact surface and possibly by mechanical “interlocking” [9] between film/substrate caused by roughening of the substrate.

However, it is important to mention that the increase in the roughness of the film above the 240 grit surfaces lead to a decrease in the critical load due to an increase in the coefficient of friction during the scratch test [57]. The increased coefficient of friction increased the tangential forces and hence the shear stresses available for film detachment. This may explain the lower values of critical load found in the very rough (grit blasted) samples compared to the smoother, 240 grit, surface.

Substrate surface cleanliness before coating showed a significant increase in the adhesion between film and substrate (Figure 4.18). Cleanliness of the substrate was believed to remove all impurities and oxides particles from the surface which, if present between film and substrate, will act as an initiation site for cracks at the interface. In general, it was reported [51, 108] that better the adhesion was observed in samples with increase cleanliness (See for example Figure 5.6).

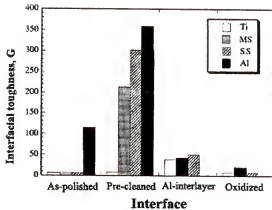


Figure 5.6 Experimental data shows the effect of pre-cleaning on the interfacial toughness of DLC coatings deposited on different substrates [110].

Pre-oxidation of the Zircaloy substrate at high temperature, 1200°C produced very thick oxide layer with intensive cracking at the interface. Cracks at the interface were attributed to the high compressive residual stresses generated in the film during the transformation from Zr to  $\text{ZrO}_2$  with a dramatic volume increase since the volume dilatation equals approximately 1.5. Because  $\text{ZrO}_2$  has very high fracture toughness, no cracks were observed to propagate through the oxide layer, and most of the cracks were found along the interface as shown in Figure 4.11(d). The fracture toughness for zirconia is approximately  $12 \text{ MPa m}^{1/2}$  which is twice of that for SiC.

Diffusion of oxygen ions through grain boundary of  $\text{ZrO}_2$  grains, Figure 4.13, could be also accelerated in the case of such small equiaxed grains due to the increase of the number of diffusion paths. Intergranular corrosion in these grains was observed when the oxidized samples were exposed to the high temperature autoclave conditions (Figure 5.7).

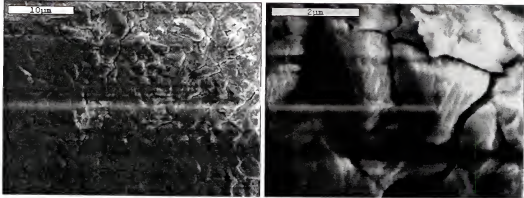


Figure 5.7 Low and high magnification SEM images show intergranular corrosion in zirconia layer after autoclave testing.

### Work of Adhesion

Most of the models which are used to calculate the practical work of adhesion were based on evaluation of the energy required to debond the film from the substrate. However, plastic deformation in the film and the substrate will absorb a significant amount of the applied energy [74, 76, 111] and therefore the calculated energy will be much higher than the actual work of adhesion .

The small values of work of adhesion between SiC films and Zircaloy-4 substrate ( $<2 \text{ J/m}^2$ ) were found in many ceramic/ metal coating systems which do not have strong bonding. Similar low values of the interfacial energy were found in thin Cu and Cr films ( $0.3\text{-}0.8 \text{ J/m}^2$ ) on glass using the same model for energy calculation [112]. Benjamin and Weaver [52] suggested that the adhesion between metal films and glass substrate was attributed entirely to weak van der Waals forces.

The main difference between the Laugier and Bull-Rickerby Models, which were used for the calculation of the work of adhesion, were that the former incorporates the residual stresses in the calculation of the total stresses required for decohesion [109]. Laugier also considered the effect of the friction between the stylus and the coating

surface. However, friction is already related to the critical load and it was found experimentally that an increase in roughness decreased the critical load. A relationship has been [56] derived between the normal applied load,  $P$ , and the coefficient of friction,  $\mu$ :

$$P \propto w^2/\mu \quad (5.2)$$

where  $w$  is the scratch width. Since the stresses applied in the front of the stylus are compressive, the compressive residual stresses stored in the SiC films contributed to the total energy required for debonding when the Laugier model was used. This explains the lower values of work of adhesion from the Laugier model as compared to that from the Bull-Rickerby model. Even lower values of work of adhesion would be expected if other residual stresses could be estimated, for example, residual stresses in amorphous silicon carbide coatings were found to be generated from the incorporation of hydrogen and was a function of the amount of hydrogen in the coating. Another possible source of residual stresses is the low energy ion bombardment during the deposition process [109, 113]. It should also be noted that these models will give better estimate of work of adhesion for brittle films deposited on brittle substrates due to lower plastic deformation encountered in both films and substrates. This low value of work of adhesion in the SiC coatings used in this study explains the adhesive type of failure which were seen by SEM and EDS analysis of scratched coatings in this study.

The comparison between the heat-treated and the untreated samples gave a good estimate of the adhesion difference between the two samples when scratch tests were used. The two samples were exactly the same, in regard to the substrate preparation and coating conditions, and the same scratch test parameters were also the same. Therefore,

the only difference between these samples was in thermal treatment after coating. The increase in the critical loads and, hence, work of adhesion for coatings after heat treatment was attributed to the relief of the compressive residual stresses where, in this case, more stresses were required to detach the film. It was shown [113] that the coating residual stresses of PE-CVD SiC films gradually changes from compressive to tensile during annealing (Figure 5.8).

The stresses responsible for coating detachment [114] were a combination of the residual stress remaining in the coating at room temperature, and the stresses introduced by the scratch stylus. Therefore, the higher adhesion strength found in heat treated samples could be attributed to the relief of residual compressive stresses in the coatings.

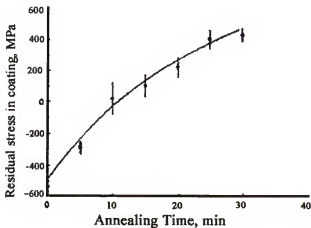


Figure 5.8 Residual stresses in PE-CVD SiC coatings on steel vs. annealing time at 923K [113].

The weak interfacial toughness between SiC films and Zircaloy-4 was attributed mainly to the deposition at low temperatures. The high temperature deposition was avoided to prevent any microstructural changes or degraded mechanical properties of the Zircaloy substrate. It was found that heating the Zircaloy near the  $\alpha$ - $\beta$  transformation temperature resulting in the formation of the secondary phase particles to the grain

boundaries (Figure 5.9), which lead to detrimental effects on the ductility and corrosion resistance [115].

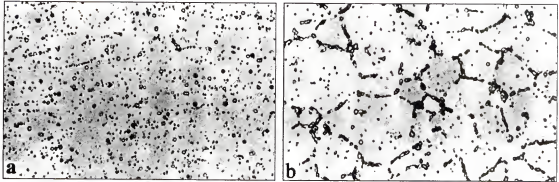


Figure 5.9 Zircaloy-4 thick sheet after thermal annealing (a) at 730°C showing the iron-chromium phase precipitated throughout the matrix, (b) at 900°C showing the iron-chromium phase precipitated into the grain boundaries (1200X) [116].

#### **Analytical Techniques for Coating Characterization**

The scratch test is the most commonly used technique for adhesion assessment and the measurement of the critical load of failure, which was found to be accurate and reproducible and a good agreement between the acoustic emission and friction force detection was found (Figure 4.5 (b)). However, it is still hard to get quantitative or even good qualitative values of adhesion. Different testing parameters and/or coating conditions give different values of critical loads which do not always represent the actual adhesion. For example, the lower critical loads value found in sample E1, which had very rough substrate surface (Grit blasted), was attributed to the high friction between stylus and surface and not necessary to the lower adhesion. Furthermore, adhesion between film and substrate is usually tested at room temperature which may not represent the actual adherence at high temperatures. For example, elastic modulus, strength, and interfacial toughness can change [44] as the temperature is increased which may affect the adhesion. Also, adhesion may increase or decrease with time as reported by Benjamin

and Weaver [52] in the effects of aging of different coatings on their adhesion to the substrate.

X'Pert is a powerful X-ray technique for measurement of residual stresses in thin films. However, because SiC films were amorphous, this technique could not be utilized to measure the stresses in the film.

Auger Spectroscopy, on the other hand, is a good technique for interface composition characterization, but is not very helpful for rough surfaces (e.g. 600 grit and higher) due to large scattering. The surface should be very smooth (polished to  $\ll 1\mu\text{m}$ ) for acceptable measurements.

### **Ultimate Tensile Shear Strength of the Coatings**

Tensile test results indicated (Figure 4.40) detachment of SiC films occurred at relatively low strains (2%). It was found [94] that only when the interface has relatively high toughness that the film remains fully attached to the substrate even at high strains and multiple cracking.

Moreover, the effect of residual stresses in the film was not considered in the calculation of fracture strength in periodic cracking. The fracture strength with the contribution of residual stresses,  $\sigma_f$ , will be

$$\sigma_f = \sigma_{f0} + \sigma_r \quad (5.3)$$

where,  $\sigma_{f0}$  is the fracture strength determined by Hook's law. Since stress measurement in the SiC film could not be conducted by X-ray analysis due to the lack of crystallinity.

The stresses were estimated from the thermal expansion mismatch assuming that modulus and thermal expansion coefficients are independent of temperature. The deposition temperature of SiC was 350°C and room temperature was assumed to be



20°C. Therefore, the residual stresses, caused by thermal expansion mismatch between the film and the substrate, were approximately 0.064 GPa.

It can be seen from equation (1.2) that the lowest possible value for interface ultimate shear strength will be for the smallest possible fracture strength,  $\sigma_f$ , and largest crack spacing  $\lambda$ . The smallest value of  $\sigma_f$  can be calculated by using the smallest value of fracture strain, which is 2% and the largest possible residual stresses which is 1.5 GPa as estimated [109] for amorphous CVD SiC thin films deposited at 350°C. The fracture strength was then calculated to be 0.8 GPa. Substituting this value into equation (1.3), the lowest possible value for interface ultimate shear strength ( $\tau_{uss}$ ) was 0.54 GPa. Therefore, the range of  $\tau_{uss}$  is 0.54-1.54 GPa.

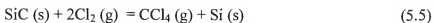
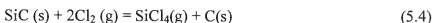
Argwal and Raj [117] reported values of  $\tau_{uss}$  for silica/ copper interface in the range 0.56-1.67 GPa. Higher value of  $\tau_{uss}$ , 9.87 GPa, was reported [118] for TiN/steel interface. The high value of  $\tau_{uss}$  for TiN/Steel was attributed to the presence of the intermetallic compounds,  $Fe_2Ti$ , formed at TiN/steel interface. No reactions or intermetallic compounds were detected at the SiO/Cu and SiC/Zircaloy interfaces, which were atomically smooth. In fact, interaction between Zircaloy-4 and SiC was found not to occur below 1000°C [119], and at 1500°C, ZrC was formed by diffusion-based reaction.

### **Failure Mechanisms of CVD SiC Coatings in Hydrothermal Test**

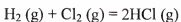
Several possibilities and mechanisms of SiC film failure in samples tested in an autoclave at 350°C and 3000 psi pressure for 24 hours were evaluated. Some of the potential mechanisms included oxidation of Zircaloy metal through pin holes in the film, formation and dissolution of  $SiO_2$  in high temperature water, and thermal stresses

generated due to heating and cooling in the autoclave which may cause film cracking and failure due to thermal expansion mismatch.

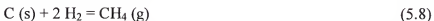
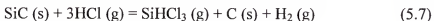
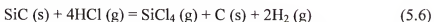
The presence of Cl in all samples in the first and second groups (A and B) may have been detrimental to the corrosion resistance of SiC film in hydrothermal conditions and was believed to be the main cause for the failure of the SiC films. It has been reported [93] that Si is preferentially attacked by chlorination of CVD SiC at 450-650°C by the reaction (s):



And when hydrogen is present in the system, HCl is formed by [120] :



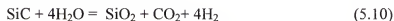
Which then react with SiC as follows:



However, when SiC films produced by trimethylsilane (without chlorine), they were also totally removed when tested in autoclave as shown in the SEM images and EDS analysis (Figs 4.25).

The other possible reason for the failure during autoclave testing was the thermal stresses which are generated in the film during the cooling in the autoclave and caused cracking and failure of the film. SEM and EDS results have shown (Figure 4.30) no effect on the film at these conditions compared to hydrothermal effects.

Hydrothermal oxidation of SiC and formation of amorphous silica (SiO<sub>2</sub>) is possible in the autoclave through the following reaction(s) [93, 121-123]:



Dissolution of silica glass in distilled water at 285°C and high pressure was reported [124] through the reaction:



Another SiC dissolution model was proposed [125] in which Si(OH<sub>4</sub>) sol, which is poorly adherent layer, produced according to the following reaction:



where Si(OH<sub>4</sub>) is then dissolved according to the reaction:



This mechanism was used [93] for the formation of a 2 μm thick carbon film on SiC fibers by hydrothermal leaching of SiC at 300-450°C.

However, the material used in the above studies was sintered SiC. It was reported [126] that CVD SiC has much lower dissolution rates and weight loss at high temperature water, 360°C, even after 7 days exposure as shown in Figure 5.10. Also, in the SiC leaching treatment [93] mentioned above, only very thin (<100nm) carbon film was obtained after hydrothermal treatment of CVD SiC in the temperature range from 550°C to 700°C under 100 MPa.

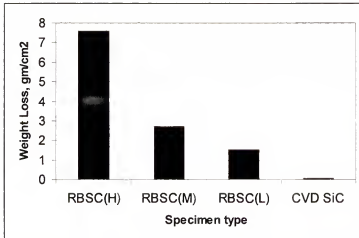
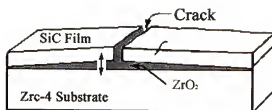
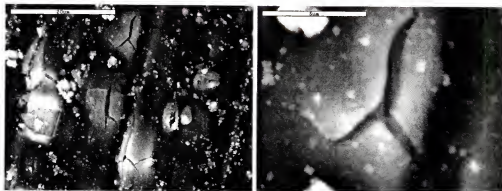


Figure 5.10 Weight loss of different types of reaction-bonded silicon carbide (RBSC) compared with CVD SiC after exposure at 360°C for 7 days in pure water. H, M and L refer to the amount of free silicon as High, medium and low respectively [126].

Oxidation of Zircaloy-4, through some pinholes in the SiC film which propagates underneath the SiC film, introduces tangential and normal stresses which may cause the cracking and failure of the film. This mechanism, as shown schematically in Figure 5.11(a), was proposed, based on the morphology of the film blistering in some areas, at the early stages of film failure, as shown in Figure 5.11(b). However, EDS mapping and line scan analysis at these holes showed much lower oxygen than the surrounding film, as shown in Figure 5.12. Based on this result, this mechanism does not seem to be valid. The oxygen content of the remaining film was much higher than that in bare metal and also higher than the content of oxygen in the film before autoclave test as shown in Figure 5.13.



(a)



(b)

Figure 5.11 (a) schematic illustration for oxidation of substrate through cracks and pinholes, (b) SEM micrographs for SiC coatings at the early stages of failure in autoclave show film blistering.

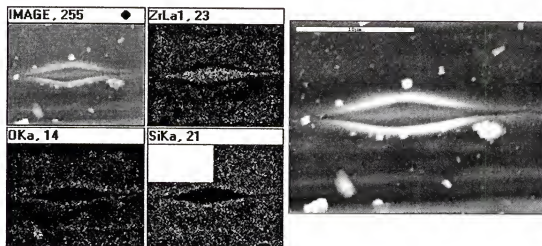


Figure 5.12 SEM and EDS map analysis show the oxygen distribution in the areas where failure begins.

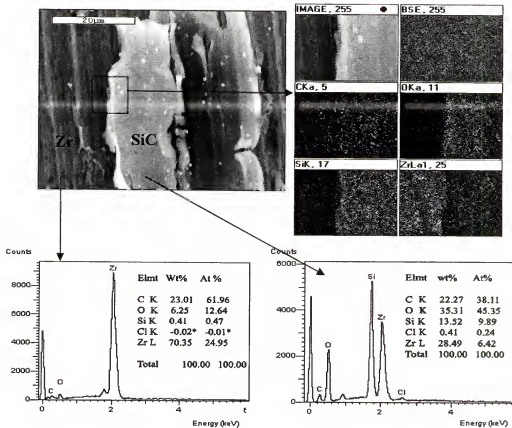


Figure 5.13 Line scan and quantitative EDS analysis of partially failed film after autoclave test shows higher oxygen contents on the SiC film than on bare Zircaloy-4 metal.

Based on the previous results and discussion and on the cracks morphology and delamination sequence, described and shown in Figure 4.26, another failure mechanism can be proposed. The transformation from SiC to SiO<sub>2</sub> through equations (5.9) to (5.12) is accompanied with increase in volume (SiC density is 3.2 gm/cc compared to 2.65 gm/cc for SiO<sub>2</sub>) which may induce compressive residual stresses lead to buckling and failure of the film as shown schematically in Figure 5.14.

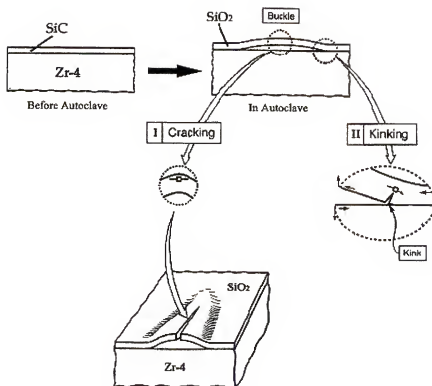


Figure 5.14 A schematic indicating the cracking and spalling phenomena that occur after buckling.

It was reported [127] that compressed films delaminate only if the film buckles. Compression stresses were found in oxidation layers formed by inward diffusion of oxygen [127]. Additional residual stresses may be formed by vapor deposition during cooling because of the thermal expansion mismatch. In addition, there are other sources of residual stresses [109, 113] in the amorphous SiC coatings that may come from the incorporation of hydrogen during deposition process and is a function of the amount of hydrogen in the coating.

Large residual compression stresses cause delamination and spalling of the thin films (Figure 2.8), where initial delamination occurs by cracks parallel to the interface followed by propagation until complete spallation of the film. Delamination of thin films occurs when energy-release rate or crack driving force equal to the fracture resistance of

the interface. However, most of the models developed for buckling and spallation due to residual compression stresses requires a pre-separation at the interface and the critical stresses for buckling is given in Equation 2.17. [127-130]

It was established [130] that large compressive stresses can cause buckling of the film when a critical separation,  $C_b$  (Figure 2.8), exists at the interface:

$$C_b = 1.1h \sqrt{\left( \frac{E_f}{(1-\nu_f^2)\sigma_b} \right)} \quad (5.16)$$

where  $h$ ,  $E_f$ ,  $\nu_f$  are thickness, Young's Modulus and Poisson's ratio of the film,  $\sigma_b$  is the residual compressive stresses. Buckling will propagate along the interface if an interfacial toughness exceeded by a critical stress given by :

$$\sigma_p = 2.5 \sqrt{\left( \frac{E_f \Gamma_i}{(1-\nu_f^2)h} \right)} \quad (5.17)$$

where  $\Gamma_i$  is the interface toughness. The corresponding critical size for buckling to propagate is:

$$C_p = 2h \sqrt{\left( \frac{E_f}{(1-\nu_f^2)\sigma_p} \right)} \quad (5.18)$$

The spallation of the buckled film will occur when cracks deflected and propagate into the film and extend to the surface. This will depend on the applied stress and on the film toughness relative to the interfacial toughness. The stress at which the spall of the film occurs is [130]

$$\sigma_s = 1.7 \sqrt{\left( \frac{E_f \Gamma_o}{(1-\nu_f^2)h} \right)} \quad (5.19)$$

where  $\Gamma_o$  is the film toughness.



Applying these mechanics for SiO<sub>2</sub> oxide layer: thickness  $h=1\mu\text{m}$ , Poisson's ratio  $\nu=0.17$ , Young's modulus  $E=73\text{ GPa}$ . The film toughness is  $\Gamma_0=6\text{ J/m}^2$  [131]. The interfacial toughness, was calculated as  $\Gamma_i = 0.8\text{ J/m}^2$ , based on the work of adhesion calculations. The critical stresses found from Eqs. (5.17) and (5.19) are,  $\sigma_p=0.6\text{ GPa}$  and  $\sigma_s=1.2\text{ GPa}$  respectively. These values bound the average stresses estimated from residual stresses found in SiC films which are 1.5-3.0 GPa. However, for buckling to propagate, these stresses require a minimum critical pre-separation between film and substrate which were proposed to occur due to interface undulation. Compare these values with that for SiC: thickness  $h=1\mu\text{m}$ , Poisson's ratio  $\nu=0.17$ , Young's modulus  $E=212\text{ GPa}$ . The film toughness is  $\Gamma_0=20\text{ J/m}^2$  [131]. The critical stresses were calculated to be  $\sigma_p=1.2\text{ GPa}$  and  $\sigma_s=3.8\text{ GPa}$ . Furthermore, silica (SiO<sub>2</sub>) has very low value of coefficient of thermal expansion ( $\text{CTE}=0.5 \times 10^{-6}/^\circ\text{C}$ ), compared to that for SiC ( $\text{CTE}=4.8 \times 10^{-6}$ ), which will cause higher residual compressive stresses when cooled from the autoclave temperature. The minimum separation required for buckling to occur, (from Equation 5.14), is  $12\mu\text{m}$  and for spallation, Equation (5.16), is  $16\mu\text{m}$ . These values are in the range reported in the literature [86]. Stresses responsible for films debonding from Zircaloy-4 are summarized in Table 5.1.

Table 5.1 stresses data for debonding of SiC and SiO<sub>2</sub> films from Zircaloy substrate.

Property	SiO <sub>2</sub>	SiC
Fracture toughness, $\text{J/m}^2$	6	20
Buckling stress, GPa	0.6	1.13
Spallation stress, GPa	1.2	3.8
Coefficient of thermal expansion (CTE), $\times 10^{-6}/^\circ\text{C}$	0.5	4.8
Residual thermal stresses, GPa	0.15	.075

One of the possible mechanisms for initial separation, which does not require a pre-separation, is the presence of perturbations on the interface [128, 130]. It was shown [132] that even small morphological variations from the smooth planar interfaces have a large effect on the stresses at the interface enough to initiate decohesions at the interface that lead to buckling. Analysis and calculations of the energy release rates for different interface morphologies have shown that periodic morphologies "perturbations" can initiate and grow these separations, as shown in Figure 5.15, to a length sufficient for buckling. Normal stresses occur at the peaks and valleys along the interface and when the film is in compression, tensile forces act across the interface at the peaks. Consequently, plane strain cracks are considered to originate in a region of the interface in tension. It was evident from SEM images, Figure 4.26(2), that the initiation of cracks and buckling were parallel to the scratch lines. Separations, as shown in Figure 5.15, nucleated preferentially at the scratches peaks due to higher tensile stresses normal to the interface [133].

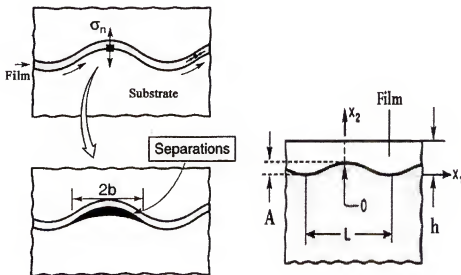


Figure 5.15 Schematic diagram shows the nucleation of separation at the undulation peak caused by tensile stresses [133].

The interface morphology was proposed to be an important factor in the formation of the initial separation that leads to buckling and spalling of compressed films [130].

The ability of this undulation to initiate and grow interface separations large enough for buckling to occur is strongly affected by their size, the stress and the interface toughness given by:

$$G = \frac{\sigma_0^2 h}{4E_f} \left( \frac{A}{h} \right)^2 \quad (5.20)$$

where A is the amplitude, h is film thickness and  $E_f$  is the Young's Modulus. The energy release rate can be calculated to predict the effects that occur in the compressed films.

The buckling will happen whenever the energy release rate exceeds the work of adhesion ( $G > W_{AD}$ ). It can be seen from this equation that the increase in the amplitude, A, which represents surface roughness, will increase the possibility of the film buckling. This may explain the partial failure that occurs in the smooth (600 grit polish) interface compared to the total failure of all other coatings with coarser interfaces. However, there is a need for more experimental work to clarify the effect of roughness on the increase in failure of oxide film in the autoclave. In summary, there are four contributions that may cause cracking and spallation of the films in autoclave: (1) compressive residual stresses associated with transformation, (2) the very low thermal expansion coefficient of  $\text{SiO}_2$  give as an additional amount of compressive residual stresses during cooling, (3) low fracture toughness of  $\text{SiO}_2$ , and (4) tensile stresses associated with interface toughness.

## CHAPTER 6

### CONCLUSIONS AND FUTURE WORK

Silicon carbide films were deposited on Zircaloy-4 using plasma-assisted chemical vapor deposition. Results for adhesion, thermal and hydrothermal stability of these films were presented and discussed. The following conclusion

- Residual stresses are very important in thin films and significantly influence the performance, reliability and integrity of the coatings. Thin films are very susceptible to cracking, buckling and spallation due to high residual stresses. A full understanding of stresses developed in thin films and mechanisms of failure is therefore essential for prediction and optimization of their life.
- Scratch testing can give useful information regarding the adhesion of coatings provided that careful understanding of the failure modes and interpretation of the results and scratch morphologies is carried out.
- Higher adhesion values were found at the intermediate level of roughness. Cleanliness of the substrate improved the adhesion. Heat treatment was also found to increase the adhesion due to relief of residual stresses in the film.
- Work of adhesion of (0.2-0.8 J/m<sup>2</sup>) and ultimate tensile shear strength of (0.54-1.54 GPa) were evaluated for SiC films.
- All SiC films were failed when tested in autoclave at high temperature and high pressure water. The failure mechanism was consistent with buckling mode of failure due to compressive residual stresses generated during oxidation of SiC coatings.

For better adhesion, deposition should be done at such energy that there is some interdiffusion of the coating material into the substrate to give a graded interface. Ion implantation prior or after SiC deposition could help to form a graded interface. Deposition at high temperatures is another way to have high interfacial toughness between coating and substrate due to atomic interdiffusion. The negative effect of the high temperatures on Zircaloy properties could be overcome by induction heat treatment

after coating to preserve the microstructural and mechanical properties. Deposition should also be carried out on smooth surfaces for better characterization of the interface.

Additional investigation of residual stresses in the thick SiC films is required to identify the tensile stresses found in such films which were expected to have compressive residual stresses.

## LIST OF REFERENCES

1. B. Lustman and F. Kerze, *The metallurgy of zirconium*. (McGraw Hill, 1955).
2. M. Parise, O. Sicardy, and G. Calletaud, *Modelling of the mechanical behavior of the metal-oxide system during Zr alloy oxidation*. Journal of Nuclear Materials, **256**(1998) 35-46.
3. W. H. Cubberly, P. M. Unterweiser, D. Benjamin, C. Kirkpatrick, V. Knoll, and K. Nieman, *Corrosion resistance of Zirconium and its alloys*. (Metals Handbook, Volume 3, 9th edition), 784-791.
4. Daniel Balint and John Hutchinson, *Zirconium and Hafnium*. International symposium on adhesion aspects of thin films.
5. Handbook Metals, *Corrosion resistance of Zirconium and its alloys*. 784-791.
6. V. Vrtlikova, J. Jaros, J. Cmakal, and L. Belovsky, *Corrosion of Zr-alloys*. An international topical meeting on high water reactor fuel performance, Apr. 10-13, (2000) 401-415.
7. J. Moya, M. Diaz, J. Bartolome, E. Roman, J. Sacedon, and J. Izquierdo, *Zirconium oxide film on Zircaloy by water corrosion*. Acta Mater., **48**(2000) 4749-4754.
8. H. Anada, K. Takeda, S. Hagi, T. Murata, A. Oe, and T. Miyachita, *Out-of-pile corrosion behavior and corrosion mechanism of NDA for high burn-up fuel of PWR*. 445-456.
9. Y. Kim, S. Bae, and T. Karlsen, *Evaluation of several effects on PWR cladding corrosion performance and modeling*.
10. J.J. Vermoyal, A. Frichet, L. Dessemond, and A. Hammou, *AC impedance study of corrosion films formed on zirconium based alloys*. Electrochimica Acta, **45**(1999) 1039-1048.
11. S. Lee, C. Park, H. Kwon, and B. Choi, *Corrosion resistance of nitrogen-implanted Zircaloy-4 in high temperature water*. Journal of Nuclear Materials, **282**(2000) 223-231.
12. G.D. Agli, C. Ferone, G. Mascolo, and M. Pansini, *Crystallization of monoclinic zirconia from metastable phases*. Solid State Ionics, **127**(2000) 223-230.

13. F. Lefebvre and C. Lemaignan, *Irradiation effects on corrosion of zirconium alloy claddings*. Journal of Nuclear Materials, **248**(1997) 268-274.
14. K. Sickafus, H. Matzke, K. Yasuda Chodak, R. Verral Lucuta, H. Andrews, A. Turos, R. Fromknecht, and N. Baker, *Radiation damage effects in cubic-stabilized zirconia irradiated with 72 MeV I ions*. Nuclear Instruments and Methods in Physics Research, **B 141**(1998) 358-365.
15. H. Okada, T. Tamura, N. Ramakrishnah, S. N. Atluri, and J. S. Epstein, *Analysis of toughening of magnesi partially stabilized zirconia, due to dilatational transformation*. Acta Metall. Mater., **40**(1992) 1421-1432.
16. K. Lam and J. Zhang, *Transformation twinning in monoclinic zirconia particles*. Acta Metall. Mater., **40**(1992) 1395-1401.
17. H. Stone, T. Kaneko, and N. Miyakawa, *In situ measurements and growth kinetics of silicon carbide chemical vapor deposition from methyltrichlorosilane*. Journal of Crystal Growth, **219**(2000) 245-252.
18. J. Hofmann and S. Veprek, *Ultra thin 3C-SiC pseudomorphic films on Si prepared by organometallic CVD with methyltrichlorosilane*. Thin Solid Films, **318**(1998) 18-21.
19. S.J. Toal, H. S. Reehal, S. J. Webb, N. Barradas, and C. Jeynes, *Structural analysis of nanocrystalline SiC thin films grown on Silicon by ECR plasma CVD*. Thin Solid Films, **343-344**(1999) 292-294.
20. G. Foti, *Silicon carbide: from amorphous to crystalline material*. Applied surface Science, **184**(2001) 20-26.
21. T. Kaneko, N. Miyakawa, H. Sone, and M. Iijima, *Thin film growth of silicon carbide from methyl-trichloro-silane by RF plasma-enhanced CVD*. Journal of.
22. S. Sivaram, *Chemical Vapor Deposition*. Van Nostrand Reinhold, 1995.
23. D. R. Cote, S. V. Nguyen, A. K. Stamper, D. S. Armbrust, D. Tobben, R. A. Conti, and G. Y. Lee, *Plasma processing*, **43**.
24. S.H. Rejeb, R. Gharbi, M. Fathallah, F. Demichelis, C. F. Pirri, E. Tresso, and G. Crovini, *Light induced defects in amorphous silicon-carbon alloys a-SiC:H*. Optical Materials, **6**(1996) 13-16.
25. I. Ferreira, A. Cabrita, E. Fortunato, and R. Martins, *Composition and structure of silicon-carbide alloys obtained by hot wire and hot wire plasma assisted technique*. Vacuum, **64**(2002) 261-266.

26. I. Ferreira, V. Silva, E. Fortunato, and R. Martins, *Mass spectroscopy analysis during the deposition of a-SiC:H and a-C:H films produced by hot wire and hot wire plasma-assisted techniques*. Applied Surface Science, **184**(2001) 60-65.
27. J. Koskinen, R. J. Soava, and H. H. Johnson, *Small-scale high strength silicon carbide fibers fabricated from thin films produced by plasma-enhanced chemical vapor deposition*. J. Vac. Sci. Tech., **A 8**(3)(1990) 1422-1426.
28. I. Ferreira, M. E. V. Costa, L. Pereira E. Fortunato, R. Martins, A. R. Ramos, and M. F. Silva, *Silicon carbide alloys produced by hot wire, hot wire plasma-assisted and plasma-enhanced CVD techniques*. Applied Surface Science, **184**(2001) 8-19.
29. K. Yamamoto, Y. Ichikawa, N. Fukada, T. Nakayama, and Y. Tawada, *Physical properties and structure of carbon-rich a-SiC films prepared by r.f. glow discharge decomposition*. Thin solid films, **173**(1989) 253.
30. F. Demichelis, G. Grovini, C. F. Pirri, E. Tresso, R. Galloni, R. Rizzoli, and C. Summonte Rava, *Optimization of relevant deposition parameters for high quality a-SiC:H films*. Solar Energy Materials and Solar Cells, **37**(1995) 315-321.
31. G.V. Rusakov, L. A. Ivashchenko, V. I. Ivashchenko, and O. K. Porada, *Peculiarities of preparing a-SiC:H films from methyltrichlorosilane*. Applied Surface Science, **184**(2001) 128-134.
32. T. Kaneko, N. Miyakawa, H. Stone, and H. Yamazakia, *The growth process and optical spectroscopy of amorphous silicon carbide films from methyltrichlorosilane by rf plasma CVD*. Surface and Coatings Technology, **142-144**(2001) 360-364.
33. G. Ziegenbalg, U. Breuel, E. Ebrech, and H. Holldorf R. Brink, *Synthesis of -silicon nitride powder by gas-phase ammonolysis of CH<sub>3</sub>SiCl<sub>3</sub>*. Journal of the European Ceramic Society, **21**(2001) 947-958.
34. L. Calcagno, M. F. Roccaforte, C. Bongiorno, and G. Foti, *Crystallisation mechanisms of amorphous silicon carbide*. Applied Surface Science, **184**(2001) 123-127.
35. M. Delplancke, J. M. Powers, G. J. Vandentop, and G. A. Somorjai, *Preparation of SixC<sub>7</sub>H<sub>7</sub> films from methylsilane by plasma-enhanced chemical vapor deposition*. Thin solid films, **202**(1991) 289-298.
36. Y.M. Lu and I. C. Leu, *Microstructural study of residual stress in chemically vapor deposited -SiC*. Surface and Coatings Technology, **124**(2000) 262-265.
37. Y. M. Lu and I. C. Leu, *Qualitative study of beta silicon carbide residual stress by Raman spectroscopy*. Thin Solid Films, **377-378**(2000) 389-393.



38. B. Reznik, D. Gerthsen, W. Zhang, and K. Hutter, *Microstructure of SiC deposited from methyltrichlorosilane*. Journal of the European Ceramic Society, **23**(2003) 1499-1508.
39. I.C. Leu, Y. Lu, and M. Hon, *Substrate effect on the preparation of silicon carbide whiskers by chemical vapor deposition*. Journal of Crystal Growth, **167**(1996) 607-611.
40. M. Kartz, D. Itzhak, A. Grill, and R. Avni, *Deposition of silicon carbide coatings on titanium alloy with a low pressure r.f. plasma*. Thin solid films, **72**(1980) 597.
41. F. Demichelis, G. Crovini, C. F. Pirri, E. Tresso, E. Giamello, and G. DellaMea, *Hydrogen evolution in a amorphous silicon carbide*. Physica, **B 170**(1991) 149-152.
42. F. Loumagne, F. Langlais, and R. Naslain, *Experimental kinetic study of the chemical vapour deposition of SiC-based ceramics from CH<sub>3</sub>SiCl<sub>3</sub>/H<sub>2</sub> gas precursor*. Journal of Crystal Growth, **155**(1995) 198-204.
43. H. Windischmann, *Intrinsic stress and mechanical properties of hydrogenated silicon carbide produced by plasma-enhanced chemical vapor deposition*. J. Vac. Sci. Technol., **A 9**(1991) 2459-2463.
44. S. D. Brown, *Adherence failure and measurement: some troubling questions*. Adhesion Measurements of Films and Coatings, (1995) 15-39.
45. J. Valli, *A review of adhesion test methods for thin hard coatings*. J. Vac. Sci. Tech., **A4**(6) (1986) 3007-3014.
46. J. E. Pawel and C. Hargue, *Analysis of pull tests for determining the effects of ion implantation on the adhesion of iron films to sapphire substrates*. Adhesion Measurements of Films and Coatings, (1995) 323-330.
47. G. W. Critchlow, J. Hampshire, R. Kingdon, Z. Naeem, A. B. Smith, and D. G. Teer, *Tribology International*, **30**, No. 7(1997) 499-506.
48. J. Valli and U. Makela, *TiN coating adhesion studies using the scratch test method*. J. Vac. Sci. Tech., **A3**(6)(1985) 2411-2414.
49. Andrieux, M. Ducarroir, and E. Beurprez, *Behavior of radio frequency PACVD bilayers (SiC/TiN) on steel*. Thin Solid Films, **324**(1998) 141-150.
50. B. Ollivier and A. Matthews, *Adhesion of diamond-like carbon films on polymers: an assessment of the validity of the scratch test technique applied to flexible substrates*. Adhesion Measurements of Films and Coatings, (1995) 103-114.

51. Benjamin and C. Weaver, *Measurement of adhesion of thin films*. Proc. R. Soc. London, **A254**(1960) 163-176.
52. Benjamin and C. Weaver, *Adhesion of metal films to glass*. Proc. R. Soc. London, **A254**(1960) 177-183.
53. A. Perry, *Adhesion of the chemically vapor-deposited hard coatings to steel - The scratch test*. Thin Solid Films, **78**(1981) 77-93.
54. A. Perry, *Adhesion studies of ion-plated on steel*. Thin Solid Films, **81**(1981) 357-366.
55. D. Butler and C. Stoddart Stuart, *The stylus or scratch method for thin film adhesion measurement: some observation and comments*. J. Phys. D: Appl. Phys., **D 3**(1970) 877-883.
56. F. Ashrafizadeh, *Adhesion evaluation of PVD coatings to aluminum substrate*. Surface and Coatings Technology, **130 (2)**(2000) 186-194.
57. S. J. Bull, *Can scratch testing be used as a model for the abrasive wear of hard coatings*. Wear, **233-235**(1999) 412-423.
58. Zhongwei Xie, Jing Zhu, and Wei Guo, *The scraping test and adhesion measurement of diamond and nickel electrolysis coatings*. Materials Characterization, **44**(2000) 347-352.
59. S. Amada and T. Hirose, *Influence of grit blasting pre-treatment on the adhesion strength of plasma sprayed coatings: fractal analysis of roughness*. Surface and Coatings Technology, **102**(1998) 132-137.
60. Benjamin and C. Weaver, *The adhesion of metals to crystal faces*. Proc. R. Soc. London, **A274**(1960) 267-273.
61. D. Wang and M. Chiu, *Characterization of TiN coatings post treated by metal-plasma ion implantation process*. Surface and Coatings Technology, **156**(2002) 201-207.
62. K. Walter, M. Nastasi, and C. Munson, *Adherent diamond-like carbon coatings on metals via plasma source ion implantation*. Surface and Coatings Technology, **93**(1997) 287-291.
63. C. Chang and D. Wang, *Characterization of surface enhancement of carbon ion-implanted TiN coatings by metal vapor vacuum arc ion implantation*. Nuclear Instruments and Methods in Physics Research, **B 194**(2002) 463-468.
64. B. Liu, B. Jiang, Y. Fu, D. Cheng, X. Wu, and S. Yang, *Alumina, aluminum nitride and aluminum composite coating on 0.45%C steel by using plasma source implantation and deposition (PSII&D)*. Thin solid Films, **349**(1999) system.

65. Y.P. Sharkeev, B.P.Gritsenko, S.V. Fortuna, and A.J. Perry., *Modification of metallic materials and hard coatings using metal ion implantation*. Vacuum, **52**(1999) 247-254.
66. A. Pan and J. E. Greene, *Interfacial chemistry effects on the adhesion of sputter-deposited TiC films to steel substrates*. Thin Solid Films, **97**(1982) 79-89.
67. F.S. Shieu, R. Raj, and S. L. Sass, *Control of the mechanical properties of metal-ceramic interfaces through interfacial reactions*. Acta metal. Mater., **38**(11)(1990) 2215-2224.
68. M. D. Thouless, *An analysis of spalling in the microscratch test*. Engineering Fracture Mechanics, **61**(1998) 75-81.
69. S. Venkataraman, D. L. Kohlstedt, and W. W. Gerberich, *Microscratch analysis of the work of adhesion for Pt thin films on NiO*. Journal of Materials Research, **7**(1992) 1126-1132.
70. M. T. Laugier, *An energy approach to the adhesion of coating using the scratch test*. Thin Solid Films, **117**(1984) 243-249.
71. E. suhir, *An approximate Analysis of stresses in multilayered elastic thin films*. Journal of Applied Mechanics, **55**(1988) 143-149.
72. E. suhir, *Interfacial stresses in bimetal thermostats*. Journal of Applied Mechanics, **56**(1989) 595-599.
73. M.R. Begley, D. R. Mumm, A. G. Evans, and J. W. Hutchinson, *Analysis of a wedge impression test for measuring the interface toughness between films/coatings and ductile substrates*. Acta Mater., **48**(2000) 3211-3220.
74. D.E. Packham, *Work of adhesion: contact angles and contact mechanics*. Int. J. Adhesion and Adhesives, **16**(1996) 121-128.
75. A.A. Volinsky, N.R. Moody, and W.W. Gerberich, *Interfacial toughness measurements for thin films on substrates*. Acta Materialia, **50**(2002) 441-466.
76. M.D. Coghill, *Scratch adhesion testing of soft metallic coatings on glass*. Surface and Coatings Technology, **41**(1990) 135-146.
77. S.Bull and D. Rickerby, *New developments in the in the modelling of the hardness and scratch adhesion of thin films*. Surface and Coatings Technology, **42**(2)(1990) 149-164.
78. J.S. Wang, Y. Sugimura, A. G. Evans, and W. K. Tredway, *The mechanical performance of DLC films on steel substrates*. Thin Solid Films, **325**(1998) 163-174.

79. D.C. Agrawal and R. Raj, *Measurement of the ultimate shear strength of a metal-ceramic interface*. Acta metal. 37(4), (1989) 1265-1270.
80. F.S. Shieu and M. H. Shiao, *Measurement of the interfacial mechanical properties of a thin ceramic coating on ductile substrates*. Thin Solid Films, **306**(1997) 124-129.
81. M.H. Shiao and F. S. Shieu, *Interfacial mechanical properties and fracture morphology of a TiN coated steel wire upon tensile loading*. Thin Solid Films, **358**(2000) 159-165.
82. K. Bhanumurthy and R. Schmid-Fetzer, *Interface reactions between SiC/Zr and development of zirconium base composites by in-situ solid state reactions*. Scripta Materialia, **45**(2001) 547-553.
83. S. Gorsse and Y. Le Petitcorps, *A new approach in the understanding of the SiC/Ti reaction zone composition and morphology*. Composites, **29A**(1998) 1221-1227.
84. Jae-Yeop Shim, Joon-Seop Kwak, Eung-Jun Chi, Hong-Koo Baik, and Sung-Man Lee, *Formation of amorphous and crystalline phases, and phase transition by solid-state reaction in Zr/Si multilayer thin films*. Thin Solid Films, **269**(1995) 102-107.
85. Y. Miyagawa, S. Nakao, L.S. Wielunski, H.Hasegawa, and S.Miyaqawa, *Depth profiling of nitrogen implanted into Si/C and Zr/ C bilayers with nuclear reaction analysis*. Nuclear Instruments and Methods in Physics Research, **161-163**(2000) 997-1001.
86. M.Y. He, A. G. Evans, and J. W. Hutchinson, *Effects of morphology on the decohesion of compressed thin films*. Materials Science and Engineering, **A245**(1998) 168-181.
87. A.G. Evans and J. W. Hutchinson, *On the mechanics of delaminataion and spalling in compresses films*. Int. J. Solids Structures, **20**(1984) 455-466.
88. M.Y. He and A. G. Evans, *The strength and fracture of metal/ceramic bonds*. Acta metal. Mater, **39**(1991) 1587-1593.
89. V. Teixeira, *Residual stress and cracking in thin PVD coatings*. Vacuum, **64**(2002) 393-399.
90. A.G. Evans, M. D. Drory, and M. S. Hu, *The cracking and decohesion of thin films*. J. Mater. Res., **3** (5)(1988) 1043-1049.
91. G.Q. Tong, K.C. Chan, L. Gao, and Z.R. Lin, *The grain size dependency of compressive deformation of a superplastic 3 mol% yttria stabilized tetragonal zirconia*. Materials Science and Engineering, **A336**(2002) 263-269.

92. Xin Guo and Zaoli Zhang, *Grain size dependent grain boundary defect structure: case of doped zirconia*. Acta Materialia, **51**(2003) 2539-2547.
93. Y.G. Gogotsi, S. Welz, J. Dagfal, M.J. McNallan, I.D. Jeon, K.G. Nickel, and T. Kraft, *Formation of carbon coatings on SiC fibers by selective etching in halogens and supercritical water*. Ceramic Engineering & Science Proceedings, **19**(3) (1998) 87-94.
94. Y. Sugimura A. G. Evans W. K. Tredway J.S. Wang, *The mechanical performance of DLC films on steel substrates*. Thin Solid Films, **325**(1998) 163-174.
95. U. Makela J. Valli, *TiN coating adhesion studies using the scratch test method*. J. Vac. Sci Tech., **A3**(6)(1985) 2411-2414.
96. C. Stoddart Stuart D. Butler, *The stylus or scratch method for thin film adhesion measurement: some observation and comments*. J. Phys. D: Appl. Phys., **D 3**(1970) 877-883.
97. B. Velde, *Structure of surface cracks in soil and muds*. Geoderma, **93**(1999) 101-124.
98. R. Huang J. Liang, J.H. Prevost, Z.Suo, *Evolving crack patterns in thin films with the extended finite element method*. International Journal of Solids and structures, **40**(2003) 2343-2354.
99. Z. Suo, *Fracture in thin films*. (2000).
100. F. Erdogan G. Schulze, *Periodic cracking of elastic coatings*. Int. J. Solids Structures, **35**(28-29) (1998) 3615-3634.
101. A. Ozturk T. Bhatia, L. Xie, E. Jordan, *Mechanisms of ceramic coating deposition in solution-precursor plasma spray*. J. Mater. Res., **17**(9) (2002) 2363-2372.
102. N. Klingbeil J. Beuth, *Cracking of thin films bonded to elastic plastic substrates*. J. Mech. Phys. Solids, **44**(9) (1996) 1411-1428.
103. D. Clarke P. Tavernier, *Mechanics of laser-assisted debonding of films*. Journal of Applied Physics, **89**(2001) 1527-1536.
104. P. Olivi E. Rodriques, *Preparation and characterization of Sb-doped SnO<sub>2</sub> films with controlled stoichiometry from polymeric precursors*. Journal of Physics and Chemistry of solids, **in press**(2003).
105. T.J. Garino and H.K. Bowen, *Deposition and sintering of particle films on a rigid substrate*. J. Am. Ceram. Soc., **70**(11) (1987) 315-317.

106. Sang-Kwon Park Myung-Chan Jo, Sang-Joon Park, *A study on resistance of PECVD silicon nitride thin film to thermal stress-induced cracking*. Applied surface Science, **140**(1999) 12-18.
107. C. Lo W. Fang, *On the thermal expansion coefficients of thin films*. Sensors and Actuators, **84**(2000) 310-314.
108. T. Fukushima S. Kuroda, S. Kitahara, *Generation mechanisms of residual stresses in plasma-sprayed coatings*. Vacuum, **41**(4-6) (1990) 1297-1299.
109. R.F. Davis K.A. Gruss, *Adhesion measurement of zirconium nitride and amorphous silicon carbide coatings to nickel and titanium alloys*. Surface and Coatings Technology, **114**(1999) 156-168.
110. T.W. Clyne X.L. Peng, *Mechanical stability of DLC films on metallic substrates Part II - Interfacial toughness, debonding and blistering*. Thin Solid Films, **312**(1998) 219-227.
111. G. Lucas A. Bagchi, Z. Suo, A. Evans, *A new procedure for measuring the decohesion energy for thin ductile films on substrates*. J. Mater. Res., **9**(7) (1994) 1734-1741.
112. A. Bagchi, G. Lucas, Z. Suo, and A. Evans, *A new procedure for measuring the decohesion energy for thin ductile films on substrates*. J. Mater. Res., **9**(7) (1994) 1734-1741.
113. M. Chen T.Z. Kattamis, *Effect of residual stresses on the strength, adhesion and wear resistance of SiC coatings obtained by plasma-enhanced chemical vapor deposition on low alloy steel*. Surface and Coatings Technology, **70**(1994) 43-48.
114. S.J. Bull, *Failure mode maps in the thin film scratch adhesion test*. Tribology International, **30**(7) (1997) 491-498.
115. J. Schemel, *Introduction to zirconium and its alloys*. 781-784.
116. P. Danielson, *Zirconium and Hafnium and their alloys*. (Metals Handbook, Volume 2, 9th edition, 1980), 498-502.
117. R. Raj D.C. Agrawal, *Measurement of the ultimate shear strength of a metal-ceramic interface*. Acta metal. **37**(4), (1989) 1265-1270.
118. f S. Shieu M.H. Shiao, *Interfacial mechanical properties and fracture morphology of a TiN coated steel wire upon tensile loading*. Thin Solid Films, **358**(2000) 159-165.
119. R. A. Verral, M.D. Vljajic, and V.D. Krstic, *Silicon carbide as an inert-matrix for a thermal reactor fuel*. Journal of Nuclear Materials, **274**(1999) 54-60.

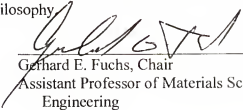
120. Y. Gogotsi, I. Jeon, and M. McNallan, *Carbon coatings on silicon carbide by reaction with chlorine-containing gases*. J. Mater. Chem., **7**(9) (1997) 1841-1848.
121. Y.G. Gogotsi N.S. Jacobson, M. Yoshimura, *Thermodynamic and experimental study of carbon formation on carbides under hydrothermal conditions*. J. Mater. Chem., **5**(4) (1995) 595.
122. S.C. Singhal, *Effect of water vapor on the oxidation of hot-pressed silicon nitride and silicon carbide*. J. Am. Ceram. Soc., **59**(1976) 81-82.
123. P.J. Jorgensen, M.E. Wadsworth, and I.B. Cutler, *Oxidation of silicon carbide*. J. Am. Ceram. Soc., **42**(12) (1959) 613-616.
124. N.S. Jacobson, Y.G. Gogotsi, and M. Yoshimura, *Thermodynamic and experimental study of carbon formation on carbides under hydrothermal conditions*. J. Mater. Chem., **5**(4) (1995) 595.
125. h.Hirayama, T. Kawakubo, and A. Goto, *Corrosion behavior of silicon carbide in 290C Water*. J. Am. Ceram. Soc., **72**(11) (1989) 2049-2053.
126. H. Hwang W. Kim, J. Park, *Corrosion behavior of reaction-bonded silicon carbide ceramics in high-temperature water*. Journal of materials science letters, **21**(2002) 733-735.
127. J. W. Hutchinson A.G. Evans, *On the mechanics of delaminataion and spalling in compresses films*. Int. J. Solids Structures, **20**(1984) 455-466.
128. A. G. Evans J.S. Wang, *Effects of strain cycling on buckling, cracking and spalling of a thermally grown alumina on a nickel-based bond coat*. Acta Mater., **47**(2) (1999) 699-710.
129. M. D. Drory M. S. Hu A.G. Evans, *The cracking and decohesion of thin films*. J. Mater. Res., **3** (5)(1988) 1043-1049.
130. A. G. Evans J. W. Hutchinson M.Y. He, *Effects of morphology on the decohesion of compressed thin films*. Materials Science and Engineering, **A245**(1998) 168-181.
131. Z. Suo T. Ye, A. Evans, *Thin film cracking and the roles of substrate and interface*. Int. J. Solids Structures, **29**(21) (1992) 2639-2648.
132. A.G. Evans, M.Y. He, and J. W. Hutchinson, *Effect of interface undulations on the thermal fatigue of thin films and scales on metal substrates*. Acta Mater., **45**(9) (1997) 3543-3554.
133. J.S. Wang and A. G. Evans, *Effects of strain cycling on buckling, cracking and spalling of a thermally grown alumina on a nickel-based bond coat*. Acta Mater., **47**(2) (1999) 699-710.

## BIOGRAPHICAL SKETCH

Yousif Al-Olayan was born in Madinah, Saudi Arabia. He obtained his bachelor's degree in mechanical engineering at King Saud University, Riyadh, Saudi Arabia. He joined the Metals R&D department in Saudi Basic Industrial Corporation (SABIC). After five years working in the R&D, he was sent by his company to the United Kingdom where he obtained his master degree in metallurgy from the University of Sheffield. He went back to Saudi Arabia and stayed there one year before he was sent to the United States to continue his higher education and get a PhD in materials science and engineering at the University of Florida. He is married and father of two sons and one daughter.



I certify that I have read this study and that in my opinion it conforms to acceptable standards of scholarly presentation and is fully adequate, in scope and quality, as a dissertation for the degree of Doctor of Philosophy.



Gerhard E. Fuchs, Chair

Assistant Professor of Materials Science and Engineering


I certify that I have read this study and that in my opinion it conforms to acceptable standards of scholarly presentation and is fully adequate, in scope and quality, as a dissertation for the degree of Doctor of Philosophy.



Ronald H. Baney

Associate Engineer of Materials Science and Engineering

I certify that I have read this study and that in my opinion it conforms to acceptable standards of scholarly presentation and is fully adequate, in scope and quality, as a dissertation for the degree of Doctor of Philosophy.



Paul H. Holloway

Distinguished Professor of Materials Science and Engineering

I certify that I have read this study and that in my opinion it conforms to acceptable standards of scholarly presentation and is fully adequate, in scope and quality, as a dissertation for the degree of Doctor of Philosophy.



Darryl P. Butt

Associate Professor of Materials Science and Engineering

I certify that I have read this study and that in my opinion it conforms to acceptable standards of scholarly presentation and is fully adequate, in scope and quality, as a dissertation for the degree of Doctor of Philosophy.



James S. Tulenko

Professor of Nuclear and Radiological Engineering

This dissertation was submitted to the Graduate Faculty of the College of Engineering and to the Graduate School and was accepted as partial fulfillment of the requirements for the degree of Doctor of Philosophy.

August 2003



---

Pramod P. Khargonekar  
Dean, College of Engineering

---

Winfred M. Phillips  
Dean, Graduate School